

# Atmospheric data support a multi-decadal shift in the global methane budget towards natural tropical emissions

Alice Drinkwater<sup>1,2</sup>, Paul I. Palmer<sup>1,3</sup>, Liang Feng<sup>1,3</sup>, Tim Arnold<sup>2,1</sup>, Xin Lan<sup>4,5</sup>, Sylvia E. Michel<sup>6</sup>, Robert Parker<sup>7,8</sup>, and Hartmut Boesch<sup>7,8</sup>

<sup>1</sup>School of GeoSciences, University of Edinburgh, Edinburgh, UK

<sup>2</sup>National Physical Laboratory, Teddington, UK

<sup>3</sup>National Centre for Earth Observation, University of Edinburgh, Edinburgh, UK

<sup>4</sup>Cooperative Institute for Research in Environmental Sciences, University of Colorado Boulder, Boulder, CO, USA

<sup>5</sup>Global Monitoring Laboratory, National Oceanic and Atmospheric Administration, Boulder, CO, USA

<sup>6</sup>Institute of Arctic and Alpine Research, University of Colorado Boulder, Boulder, CO, USA

<sup>7</sup>National Centre for Earth Observation, Space Park Leicester, University of Leicester, UK

<sup>8</sup>Earth Observation Science, School of Physics and Astronomy, University of Leicester

**Correspondence:** Alice Drinkwater (alice.drinkwater@ed.ac.uk)

**Abstract.** We use the GEOS-Chem global 3-D model and [a two inverse methods \(the Maximum A Posteriori inverse method and Ensemble Kalman Filter\)](#) to infer regional methane ( $\text{CH}_4$ ) emissions and the corresponding carbon stable isotope source signatures, 2004–2020, across the globe using *in situ* and satellite remote sensing data. Over our study period, we find consistent evidence from both atmospheric  $\text{CH}_4$  datasets of a progressive increase of [methane- \$\text{CH}\_4\$](#)  emissions at tropical (30°N to 30°S) latitudes (+3.80 Tg/yr/yr), accompanied by a progressively [isotopically](#) lighter atmospheric  $\delta^{13}\text{C}$  signature, consistent with increasing [natural biogenic wetland](#) emissions. The [highly-resolved](#) satellite remote sensing data provide evidence of [higher spatially-resolved hotspots of methane hotspots of  \$\text{CH}\_4\$](#)  that are consistent with the location and seasonal timing of wetland emissions, limiting the hypothesis about the hydroxyl radical (OH) sink for [methane- \$\text{CH}\_4\$](#)  playing a significant role in observed global growth in atmospheric [methane- \$\text{CH}\_4\$](#) . We find that since 2004, the largest growing regional contributions (2004–2020) are from North Africa (+19.9 Tg/yr), China (+21.6 Tg/yr), and Tropical South America (+14.2 Tg/yr). To quantify the influence of our results to changes in OH, we also report regional emission estimates using an alternative scenario of a 0.5%/yr decrease in OH since 2004, followed by a 5% drop in 2020 during the first COVID-19 lockdown. We find that our main findings are robust against those year-to-year changes in OH.

## 1 Introduction

Changes in atmospheric methane ( $\text{CH}_4$ ) over the last [few](#) decades have unfolded without clear explanation, exposing inadequacies in our measurement coverage and our ability to definitively attribute those changes to individual emissions and losses. The climatic importance of atmospheric  $\text{CH}_4$  lies in its ability to absorb and emit infrared radiation at wavelengths that are relevant to outgoing terrestrial radiation. Consequently, atmospheric  $\text{CH}_4$  helps to maintain Earth's radiative balance and surface and atmospheric temperatures. [Concentrations of atmospheric-Atmospheric  \$\text{CH}\_4\$  are determined by a large range of anthropogenic,](#)

20 ~~pyrogenic~~ is derived from emissions due to thermogenic (organic matter broken down at high temperatures and pressures, mainly released during extraction and transport of fossil fuels), pyrogenic (through incomplete combustion of organic matter), and biogenic ~~emissions and losses from~~ (microbial activity) based production pathways. The main loss process is from from the hydroxyl radical (OH), ~~with minor losses from the~~ reaction with chlorine, uptake from soils, and ~~a small~~ stratospheric loss. ~~CH<sub>4</sub> is the second most abundant anthropogenic greenhouse gas and has a GWP<sub>100</sub> value of 28 (Masson-Delmotte et al., 2021~~

25 ~~), a widely used metric that estimates, for a given mass emission, the influence on capturing heat in the atmosphere over 100 years. A mass emission of CH<sub>4</sub> is therefore 28 times more powerful at capturing heat in the atmosphere than an equivalent mass emission of carbon dioxide. The global CH<sub>4</sub> growth rate was close to zero from 2000 to 2006 (Dlugokencky et al., 2020) but has since accelerated to unprecedented values, with global yearly growth rate reported by NOAA exceeding 15 ppb for the first time in 2020 and 2021 (Feng et al., 2022a)(Feng et al., 2022a). Concurrently, we are witnessing progressively~~

30 ~~lighter a progressively isotopically lighter signature of global averaged CH<sub>4</sub> (more negative global average atmospheric  $\delta^{13}\text{C}$ ), indicative of a higher proportion of microbial emissions value), possibly indicative of changing contributions of emissions sources, for example an increase in biogenic sources or a decrease in thermogenic sources (Lan et al., 2021). A growing body of work have has proposed a range of hypotheses to explain short periods of observed global and regional variations in atmospheric CH<sub>4</sub> (Turner et al., 2019). In this study, we take a step back to look at observed CH<sub>4</sub> variations from 2004 onwards,~~

35 ~~and argue that short-term to 2020, in order to capture the some of the zero-growth rate period and the subsequent increase in growth rate of CH<sub>4</sub> post-2007. We argue that monthly variations are part of a large-scale shift of predominately anthropogenic thermogenic energy emissions from high northern latitudes to microbial-biogenic emissions from the tropics, driven by Tropical North African and Tropical South American wetlands. As the global atmospheric mass balance of CH<sub>4</sub> emissions shifts further from anthropogenic to microbial sources, our ability to mitigate emissions becomes more of a challenge.~~

40 The ~~post-2006-post-2007~~ increase in atmospheric CH<sub>4</sub> has been the focus of many studies and has been attributed to different plausible hypotheses associated with changes in ~~fossil fuel, biomass burning, and wetland emissions and various emissions sources, and~~ the OH sink (Turner et al., 2019). These studies have reached their conclusions using *in situ* mole fraction observations alone or in combination with other observations, e.g. *in situ*  $\delta^{13}\text{C}$  (~~Schaefer et al., 2016; Rice et al., 2016; Nisbet et al., 2016; Fujita et al., 2016; Schaefer et al., 2016; Rice et al., 2016; Nisbet et al., 2016; Fujita et al., 2020; Lan et al., 2021; Basu et al., 2022~~), satellite ob-

45 ~~servations (Worden et al., 2017; McNorton et al., 2018; Yin et al., 2021; Feng et al., 2022b)(Worden et al., 2017; McNorton et al., 2018; Yin et al., 2021; Feng et al., 2022b), or other trace gases, using a variety of analysis methods and computational models. Typical emissions sizes and uncertainty are indicated in Table 1, adapted from Saunio et al. (2020). Our approach is unique in that, for our  $\delta^{13}\text{C}$  inversion, we are solving for the  $\delta^{13}\text{C}$  isotopic source signature of a region. From the isotopic source signature of a region, we can determine how the source balance within a region is shifting has shifted over time (i.e., towards more pyrogenic or microbial, thermogenic~~

50 ~~or biogenic sources), and so gain understanding of the geographical shifts in the CH<sub>4</sub> budget.~~

~~The reaction with the OH radical in the troposphere is the largest sink of CH<sub>4</sub>, responsible for 80% of the total CH<sub>4</sub> sink globally. Changes in OH are likely to play some may have played a role in recent changes in atmospheric CH<sub>4</sub> (Rigby et al., 2017; Turner et al., 2017) but they are unlikely to be a dominant factor the magnitude of this influence is uncertain (its short atmospheric lifetime of <1 s makes direct measurement of global variability very difficult). Chemical reactions responsible for~~

55 removing CH<sub>4</sub> from the atmosphere are faster for lighter isotopologues of CH<sub>4</sub>. This isotopic fractionation therefore leads to an atmosphere enriched in heavier isotopes relative to the globally emitted CH<sub>4</sub>. Lan et al. (2021) simulated CH<sub>4</sub> and  $\delta^{13}\text{C}$  in a 3-D chemistry transport model covering the period 1984-2016, and found that ~~proposed~~ changes in OH ~~(by Turner et al., 2017) do not align proposed by (Turner et al., 2017) are not consistent~~ with the trend of increasingly isotopically light  $\delta^{13}\text{C}$  observed in the atmospheric record, ~~due to the weak fractionation of OH~~. We explore the impact of reducing OH in a sensitivity study. The

60 first COVID-19 lockdown in 2020 corresponded to an unexpected large increase in atmospheric CH<sub>4</sub>. Studies have suggested this could be partly explained by a 3-5% reduction in OH (Miyazaki et al., 2021; Laughner et al., 2021) resulting from a large-scale reduced emissions of nitrogen oxides associated with industry. This has yet to be corroborated by satellite data that provide complementary constraints on the key emitting regions over the tropics ~~(Feng et al., 2022b), or by (Feng et al., 2022b)~~

65 Here, we calculate trends in regional CH<sub>4</sub> emissions and isotopic  $\delta^{13}\text{C}$  data-source signatures across the world, 2004-2020, using *in situ* mole fraction and  $\delta^{13}\text{C}$  data, and satellite mole fraction data. This is achieved by using three sets of inversions: two Maximum A-Posteriori inversions using ground-based data (solving separately for regional emissions and isotopic source signatures), and an Ensemble Kalman Filter inversion using GOSAT data (solving for regional CH<sub>4</sub> emissions).

In the next section, we describe the data and methods we use to quantify changes in regional CH<sub>4</sub> emissions and the

70 corresponding regional stable isotope source signatures. In section 3, we report our results of *a posteriori* regional CH<sub>4</sub> fluxes and regional  $\delta^{13}\text{C}$  isotopic signatures, including analysis of sensitivity calculations that involve different assumptions about year to year changes in the OH sink. We conclude the paper in section 4.

## 2 Data and Methods

### 2.1 *In Situ* and Satellite Remote Measurements of Atmospheric Methane

75 We use surface-level flask data as constraints on both total-regional CH<sub>4</sub> emissions and  $\delta^{13}\text{C}$  regional ~~emissions~~ CH<sub>4</sub> emissions isotopic source signatures. ~~These~~ The CH<sub>4</sub> mole fraction data are taken from 31 National Oceanic and Atmosphere Administration ~~—~~ Global Monitoring Laboratory (NOAA-GML) sites around the world (Figure 1), version 2020-07 (Dlugokencky et al., 2020). The data are monthly mean values, averaged from discrete data as collected at each site, analysed at NOAA-ESRL in Boulder, Colorado, and recorded to the NOAA 2004A standard scale (Dlugokencky et al., 2005). Up to August 2019, the

80 analysis was performed using gas chromatography (Steele et al., 1987; Dlugokencky et al., 1994; Dlugokencky et al., 2005) and since August 2019, cavity ringdown spectroscopy has been used (Dlugokencky et al., 2020). We also include data from a site in Siberia, Karasevoe (KRS), which is monitored by the National Institute for Environment Studies (NIES). This site was included to maximise geographical coverage of *in situ* data. The CH<sub>4</sub> mole fraction measurements from this site are continuous, measuring from 65 m height, covering the period 2004-2020 (Sasakawa et al., 2010). A scale factor of 0.997 is applied

85 to the NIES data in order to bring it into line with the NOAA 2004A scale (Zhou et al., 2009). The site constitutes part of the Japan-Russia Siberia Tall Tower Inland Observation Network (JR-STATION).

$\delta^{13}\text{C}$  data are similarly monthly mean values, calculated from discrete flask samples at NOAA network sites. ~~Isotopic~~, reported on the international carbon isotope scale VPDB (Vienna Pee Dee Belemnite). Isotope ratio 'delta' values represent the excess of a heavy, less abundant stable isotope (for  $\delta^{13}\text{C}$  values, carbon-13) over the light, most abundant stable isotope (carbon-12) in a sample, when compared to a standard. These measurements are useful as they are indicative of the source of the  $\text{CH}_4$ : biogenic sources are dominated by isotopically lighter signatures and thermogenic sources are dominated by isotopically heavier signatures. For the NOAA network, isotopic analysis of  $\delta^{13}\text{C}$  was performed at the University of Colorado Institute of Arctic and Alpine Research Stable Isotope Laboratory (CU-INSTAAR). They follow an isotope ratio mass spectrometry approach (Miller, 2002; Vaughn et al., 2004). The geographical locations of *in situ* ~~data-used~~ measurement sites are shown in Figure 1 and represent 1. These sites are a subset of ~~those used to collect total~~ the entire NOAA network's capacity for measuring  $\text{CH}_4$  amount fractions (10 of 32) mole fractions. The sites included in the inversion ~~are~~ (both for  $\text{CH}_4$  and  $\delta^{13}\text{C}$ ) are those that cover the entire period of the inversion (2004-2020) without significant ~~period~~ periods of measurement breaks ~~so as~~ to ensure a consistent interpretation of trends without consideration of possible biases introduced through the inclusion or exclusion of specific sites.

We also estimate  $\text{CH}_4$  fluxes for 2010-2020 from the Japanese Greenhouse gases Observing SATellite (GOSAT) that was launched in 2009. GOSAT is in a sun-synchronous orbit with an equatorial local overpass time of 13:30. Since launch, it has provided continuous global observations of dry-air atmospheric column-averaged ~~carbon dioxide~~  $\text{CO}_2$  ( $\text{XCO}_2$ ) and  $\text{CH}_4$  ( $\text{XCH}_4$ ), retrieved from shortwave infrared wavelengths that are most sensitive to changes in  $\text{CH}_4$  and  $\text{CO}_2$  in the lower troposphere (Parker et al., 2020). We use the latest (v9) proxy  $\text{XCH}_4:\text{XCO}_2$  retrievals that use spectral absorption features around the wavelength of  $1.6\ \mu\text{m}$  (Parker et al., 2020, Palmer et al., 2021), because of the smaller bias and better global coverage than those provided by the full physics retrievals. ~~Analysis shows~~ Analyses show the precision of single proxy retrieval is about 0.72%, with a global bias of 0.2% (Parker et al., 2011, 2015, 2020). In our calculations, we assume a higher observation uncertainty of 1.2%, and deduct a globally uniform bias of 0.3% to obtain better *a posteriori* agreement with the independent ground-based  $\text{XCH}_4$  data by the Total Carbon Column Observing Network (TCCON). ~~These uncertainties are detailed in Feng et al. (2022b)~~. To anchor the constraints from the proxy  $\text{XCH}_4:\text{XCO}_2$  ratio (Fraser et al., 2014; Feng et al., 2017), we also assimilate the GLOBALVIEW  $\text{CH}_4$  and  $\text{CO}_2$  data (Schuldt et al., 2021), with assumed uncertainties of 0.5 ppm and 8 ppb for *in situ* measurements of  $\text{CO}_2$  and  $\text{CH}_4$ , respectively. ~~GLOBALVIEW constitutes a combination of  $\text{CH}_4$  data from ground-based data (both flask and continuous) and aircraft data, from 54 different laboratories, combined and published by NOAA-GML (Schuldt et al., 2021)~~. Locations of the assimilated GLOBALVIEW  $\text{CH}_4$  (sub) dataset are shown in ~~Feng et al., 2022b~~ Feng et al., 2022b.

## 2.2 GEOS-Chem Atmospheric Chemistry and Transport Model

To relate  $\text{CH}_4$  emissions to atmospheric  $\text{CH}_4$  concentrations, we use v12.1 of the GEOS-Chem 3-D global chemical transport model (CTM) (Bey et al., 2001) at a horizontal resolution of  $2^\circ$  (latitude) by  $2.5^\circ$  (longitude) with 47 vertical levels from the surface to 80 km height, ~~driven by with meteorological data from~~ the MERRA-2 meteorological reanalyses (Gelaro et al., 2017) from the NASA Global Modeling and Assimilation Office (GMAO).

Our *a priori* emissions include: 1) monthly EDGAR 4.3v4.3.2 anthropogenic emissions (~~Source: European Commission, 2011~~) (Janssens-Maenhout et al., 2019) that accounts for emissions from oil and gas, coal, livestock, landfills, wastewater, rice, and other anthropogenic sources (including biofuel); 2) monthly GFED-4 biomass burning emissions (version 4.1; Randerson et al., 2017); and 3) monthly v1.0 WetCHARTs wetland emissions (Bloom et al., 2017). The Harvard-NASA Emissions Component (HEMCO) software within GEOS-Chem converts the emission inventories at their native horizontal resolution to the GEOS-Chem  $2^\circ \times 2.5^\circ$  resolution. Beyond the end of the emissions inventory, emissions are repeated yearly in a *a priori* simulation.

Table 1 shows the  $\delta^{13}\text{C}$  isotopic source signatures for the source types included in our simulations. These are extracted as mean global values from Sherwood et al. (2017), which ~~provides~~ provide a database of global ~~source signatures, isotopic source signatures that are~~ broken down into the same sectors as we employed in our simulations. However, individual source types show a wide range of source signatures (~~e.g., coal mines (Zazzeri et al., 2016)~~), and this uncertainty is reflected in the assigned uncertainty given to the *a priori* source signatures in inversion (Section 2.3). We differentiate between Arctic and tropical wetlands by applying a 10‰ isotopically lighter source signature to the Arctic source (Table 1), following Ganesan et al. (2018) who produced a global wetland source signature map based upon published  $\delta^{13}\text{C}$  data. In GEOS-Chem, we simulate isotopologues separately (i.e. for  $\delta^{13}\text{C}$ ,  $^{12}\text{CH}_4$  and  $^{13}\text{CH}_4$ ), and then calculate  $\delta^{13}\text{C}$  values. The arithmetic underlying the conversion of isotope ratios to isotopologue emissions for input to the model are detailed in Appendix A.

We include the loss of atmospheric  $\text{CH}_4$  from reaction with chlorine, soil uptake, and from oxidation by OH. We use monthly 3-D fields of OH, calculated using the full-chemistry version of GEOS-Chem, and monthly 3-D field of atomic chlorine (~~(Sherwen et al., 2016)~~) (Sherwen et al., 2016). Stratospheric loss frequency fields are determined using the NASA GMI stratospheric model (Duncan et al., 2007). Estimates of the microbial consumption of  $\text{CH}_4$  in soils is determined from Fung et al. (1991). The resulting atmospheric lifetime of  $\text{CH}_4$  against OH is 9.73 years, consistent with the observed methyl chloroform lifetime of 5.39 years. This compares well with multi-model simulations (Voulgarakis et al., 2013; Morgenstern et al., 2017) that reported global mean lifetimes of  $\text{CH}_4$  that range 7.2-10.1 yrs. In our default model configuration, none of these loss processes include interannual variations.

To account for isotopic fractionation due to loss of  $\text{CH}_4$  in the troposphere and stratosphere, we use published kinetic isotope effect values (KIEs). These values are employed to scale the reaction rate constants used in the simulations for  $^{12}\text{CH}_4$  and  $^{13}\text{CH}_4$  (Table A1). The OH and Cl sinks are handled in the hard coding of the model, whereas the soil sink is handled as a negative emission in the HEMCO file. Therefore, for the soil sink, the KIE is directly applied as a scale factor in the HEMCO configuration file (Snover and Quay, 2000; Burkholder et al., 2019).

‘Spinning up’ is an important aspect of atmospheric modelling in order for simulated mole fractions to reach equilibrium. We spin-up the model by scaling a  $\text{CH}_4$  restart file from ~~and older, coarser resolution a previous~~ GEOS-Chem model run. The restart file is at  $4 \times 5^\circ$  resolution, and originally represented 2012, but is spun up to represent 2004. The  $\delta^{13}\text{C}$  inversion uses *a posteriori* regional emissions from the  $\text{CH}_4$  inversion as a starting point, with sectoral emissions scaled as detailed in Appendix A. We then run the model over the year 2004 sixty times using the 2004 MERRA-2 meteorology and emissions, corresponding to approximately six times the chemical lifetime of  $\text{CH}_4$ . We find this is sufficient to allow mole fractions and

isotope ratios to equilibrate (not shown). We then run a single-year inversion for 2004 to optimise the  $\delta^{13}\text{C}$  and ~~total-CH<sub>4</sub>~~ values relative to ~~NOAA-ground-based~~ observations, following inverse method detailed below. The output of this short inversion is improved estimates of initial conditions for  $\delta^{13}\text{C}$  and ~~total-CH<sub>4</sub>~~, which serve as a starting point for the longer inversion we report here (2004-2020). This restart file originally represented 2012, however it is spun up over 60 years to the point where it  
 160 no longer resembles 2012 and will be representative of 2004, the starting point of the simulation.

For all our calculations, we sample GEOS-Chem at the grid ~~square-box~~ and local time that corresponds to the *in situ* and satellite remote sensing data. For the satellite data, we also apply scene-dependent averaging kernels to account for vertical structure. This approach allows us to directly compare the model with measurements. Regional trends are calculated by examining the grid ~~squares which correspond with~~ boxes which correspond to a given region on the global grid.

## 165 2.3 Inverse Methods

We use two inverse methods that reflect the volume and simplicity of the data being used. For *in situ* data we use the Maximum *A Posteriori* (MAP) inverse methods and for the more voluminous satellite data we use an ensemble Kalman filter (EnKF). For brevity, we include only the essential details about either method and refer the reader to dedicated papers.

### 2.3.1 Maximum *A Posteriori*

170 To infer regional *a posteriori* CH<sub>4</sub> fluxes and regional  $\delta^{13}\text{C}$  emissions source signatures from the atmospheric measurements of CH<sub>4</sub>, we use the Maximum *A Posteriori* solution (MAP) inverse method (Rodgers, 2000). We solve for CH<sub>4</sub> fluxes and  $\delta^{13}\text{C}$  emissions signatures from 14 geographical regions (Figure 1). This method combines *a priori* knowledge and its uncertainty with the measurements and their uncertainties, and has been used in a number of studies, e.g., Fraser et al. (2014); McNorton et al. (2018).

175 The MAP solution and the associated *a posteriori* uncertainty is described as, respectively:

$$\underline{\mathbf{x}}^a \equiv \underline{\mathbf{x}}^b + (\underline{\mathbf{H}}^T \underline{\mathbf{B}}^{-1} \underline{\mathbf{H}} + \underline{\mathbf{R}}^{-1})^{-1} \underline{\mathbf{H}}^T \underline{\mathbf{B}}^{-1} (\underline{\mathbf{y}} - \underline{\mathbf{H}} \underline{\mathbf{x}}^b), \quad (1)$$

$$\underline{\mathbf{A}} \equiv (\underline{\mathbf{H}}^T \underline{\mathbf{B}}^{-1} \underline{\mathbf{H}} + \underline{\mathbf{R}}^{-1})^{-1}, \quad (2)$$

using the conventional that lower-case and upper-case variables denote vectors and matrices, ~~respectively~~:-

$$\underline{\mathbf{x}}^a \equiv \underline{\mathbf{x}}^b + (\underline{\mathbf{H}}^T \underline{\mathbf{B}}^{-1} \underline{\mathbf{H}} + \underline{\mathbf{R}}^{-1})^{-1} \underline{\mathbf{H}}^T \underline{\mathbf{B}}^{-1} (\underline{\mathbf{y}} - \underline{\mathbf{H}} \underline{\mathbf{x}}^b),$$

180  $\underline{\mathbf{A}} \equiv (\underline{\mathbf{H}}^T \underline{\mathbf{B}}^{-1} \underline{\mathbf{H}} + \underline{\mathbf{R}}^{-1})^{-1},$

where  $\mathbf{x}$  denotes the state vector that describes the estimated quantities, which in this study includes monthly CH<sub>4</sub> fluxes and  $\delta^{13}\text{C}$  source signatures from regions across the world (Figure 1). Subscripts ‘a’ and ‘b’ denote *a posteriori* and *a priori* CH<sub>4</sub> fluxes, respectively, and superscripts ‘-1’ and ‘T’ denote matrix inverse and transpose operations, respectively. The measurement vector  $\mathbf{y}$  includes ~~either NOAA mole fraction data and the~~ CH<sub>4</sub> mole fraction or  $\delta^{13}\text{C}$  data. The matrices  $\mathbf{B}$ ,  
 185  $\mathbf{A}$ , and  $\mathbf{R}$  denote the error covariances matrices for the *a priori*, *a posteriori*, and measurements, respectively.  $\mathbf{B}$  and  $\mathbf{R}$  are



diagonal matrices. For  $\mathbf{B}$  we assume uncertainties of 50% of the regional  $\text{CH}_4$  fluxes and 15‰ for the  $\delta^{13}\text{C}$  values, and for  $\mathbf{R}$  we assume 10 ppb for the mole fraction data and 0.1‰ for the isotope data. [These uncertainties were based upon similar studies \(Fraser et al., 2014; McNorton et al., 2016\).](#) We assume a model transport error of 12 ppb, following [Feng et al. \(2022b\)](#) [Feng et al. \(2022b\)](#).

190 The Jacobian matrix  $\mathbf{H}$  describes the sensitivity of the measurements to changes in the state vector, i.e.  $\partial\mathbf{y}/\partial\mathbf{x}$ . For the [total mole fraction](#)  $\text{CH}_4$  inversion, the Jacobian matrix describes the sensitivity of mole fractions in the model to changes in regional  $\text{CH}_4$  emissions. We construct the matrix using a series of GEOS-Chem model runs. We systematically let each individual emitting region (described by the state vector) emit for one month while all other regions are emitting as normal. The individual regional source is then switched off (emissions set to zero) and the effect of this on the 3-D atmospheric  
195 ~~squares that correspond with the~~ [boxes that correspond to the location of the](#) measurement sites. The resulting mole fractions therefore describe the sensitivity of a particular measurement site to changes in a specific regional source up to three months after emission. This is repeated for every month within the inversion timescale, for every region described in the state vector.

For the  $\delta^{13}\text{C}$  inversions, the *a priori* simulation uses *a posteriori* regional emissions from the  $\text{CH}_4$  inversion as a starting  
200 point. The Jacobian matrix in this case describes the sensitivity of modelled  $\delta^{13}\text{C}$  to changes in the regional [isotopic](#) source signatures. We construct the Jacobian as the difference between a control model calculation (using the  $\text{CH}_4$  *a posteriori* regional emissions [and mean source signature values from Sherwood et al. \(2017\)](#)) and perturbed source signature model calculation for the whole study period (2004-2020). For the perturbed model calculation, we systematically perturb the [isotopic](#) source signature of each region (all of the sectors that are containing geographically within a region) ~~so that it is~~ [isotopically](#) heavier  
205 by 20‰ for the period 2004-2020. The difference between the control and perturbed run in  $\delta^{13}\text{C}$  value at the location of each measurement site is then divided by the ‰-value of  $\delta^{13}\text{C}$  perturbation for the region source signature, to understand the effect of changing a regions source signature upon the  $\delta^{13}\text{C}$  value recorded at each measurement site location. Each individual regions' model calculation is spun up separately from the control model calculation in order to account for lagging in the model.

The output from the inversion are improved estimates of regional  [\$\text{CH}\_4\$  fluxes](#) and  $\delta^{13}\text{C}$  source signatures. The model sim-  
210 ulates the global atmosphere on a  $2^\circ \times 2.5^\circ$  [horizontal](#) grid. The *a posteriori* regional ~~fluxes and~~  [\$\text{CH}\_4\$  fluxes and isotopic](#) source signatures are applied to the grid ~~squares~~ [boxes](#) in the model which correspond ~~with to~~ a given region in an *a posteriori* simulation. [The \*a posteriori\* simulation is then used to compare with the \*in situ\* data to ensure the quality of the \*a posteriori\* fit.](#)

### 2.3.2 Ensemble Kalman Filter

215 We use an Ensemble Kalman Filter (EnKF) approach in performing the inversion using satellite data, because we cannot easily evaluate the necessary matrix operations associated with an analytic inversion. Here we use an ensemble of flux perturbation pulses to represent uncertainty in our *a priori* estimate for regional monthly  [\$\text{CH}\_4\$  fluxes](#). We subsequently use a global chemistry transport model (i.e., the GEOS-Chem v12) to track the transport and chemistry processes of the tagged emission pulses in the atmosphere, to project their spreads to the observation space. With the ensemble of *a priori* flux perturbations, and the

220 simulated observation impacts, we use the Ensemble Transform Kalman Filter (ETKF) algorithm to numerically estimate the *a posteriori*  $\text{CH}_4$  fluxes and the associated uncertainties by optimally comparing the model simulation with observations (see Feng et al., 2017 for more details). To reduce the computational costs, mainly from tracking tagged emission pulses, we introduce a 4-month moving lag window for each assimilation step, because any observation has limited ability to distinguish between the signals emitted long (>4 months) before, from variations in the ambient background atmosphere (Feng et al., 2017).  
225 As a result, we are able to include a larger state vector, consisting of monthly scaling factors for 487 (476 land regions and 11 oceanic regions) regional  $\text{CH}_4$  (and  $\text{CO}_2$ ) pulse-like basis functions (Figure S1 in (Feng et al., 2022b)(Feng et al., 2022b)). We define these land sub-regions by dividing the 11 TransCom-3 (Gurney et al., 2002) land regions into 42 to 56 nearly equal sub-regions, and use the 11 oceanic regions defined by the TransCom-3 experiment. Because of their smaller sizes, we have assumed a higher uncertainty percentage (60%) for *a priori* emissions than the MAP approach described above. We also  
230 include spatial correlation with a correlation length of 500km between the sub-regions.

### 3 Results

#### 2.1 Sensitivity of Results to Changes in Assumed OH Distributions

~~Figure 2 shows the regional differences between~~To examine the sensitivity of our results to changes in assumed OH distributions, we run a single sensitivity run that is made up of two parts. First, we imposed a 0.5%/yr uniform decrease to our 3-D OH field  
235 from 2004 to 2019, following similar trends proposed by Turner et al. (2017) (who proposed a 7% reduction in OH, 2003-2016) and second, we uniformly decrease OH by 5% in 2020 to describe estimated changes due to a global-scale reduction in emissions of nitrogen oxides ( $\text{NO}_x$ ) associated with the first COVID-19 lockdown Miyazaki et al. (2021); Laughner et al. (2021). It has also been suggested that OH mole fractions may have actually increased during 2000–2016 due to increasing water vapour and  $\text{NO}_x$  in the tropics (Zhao et al., 2019), however considering the scenario under COVID-19 lockdowns in 2020, a  
240 decreasing trend over the previous years is only considered here. A similar approach to this was followed by Feng et al. (2022b) for which there is some opposition that suggests the change in OH during COVID-19 should be larger, although there is no empirical determination of this change. We then recalculate ~~a priori and a posteriori emission estimates, with absolute emissions values plotted in Figure 3. Here we show~~ emissions inferred from the ground-based data.

### 3 Results

245 ~~Figure 2 shows~~ the annual mean ~~difference between the~~ differences in regions between ~~a posteriori priori~~ and ~~the a priori posteriori~~ emissions, for both ~~NOAA and GOSAT inversion results~~ emission estimates for both ground-based and GOSAT results (absolute emissions values are plotted in Figure 3). This indicates the changes from the *a priori* emissions and allows comparison of the two independent approaches. The *a priori* emissions are constructed as detailed in Section 2.2. ~~At a~~ Focusing on 2020 (due to interest in emissions changes as a result of the COVID-19 lockdowns) on a global scale, we find increased  
250 emissions relative to *a priori* emissions of  $72.0 \pm 35.5$  Tg/yr in 2020 for the *in situ* inversion and  $61.5 \pm 37.3$  Tg/yr



higher emissions for the GOSAT inversion. The *in situ* inversion results indicate that this difference originates from tropical regions such as Tropical South America ( $+13.5 \pm 1.9$  Tg/yr in 2020), North Africa ( $+15.1 \pm 6.8$  Tg/yr, 2020) and China ( $+17.3 \pm 4.4$  Tg/yr, 2020). There are decreases relative to *a priori* emissions in 2020 in Temperate North America ( $-13.3 \pm 3.4$  Tg/yr), Southern Africa ( $-5.6$   ~~$-5.6$~~   $\pm 2.1$  Tg/yr), Temperate South America ( $-4.1 \pm 4.0$  Tg/yr) and Boreal Eurasia ( $-2.3 \pm 3.9$  Tg/yr).  
255 ~~Therefore, the estimates from bottom-up inventories underestimate  $\text{CH}_4$  emissions, especially in tropical regions.~~ According to these results, mid-latitudinal emissions are being overestimated and tropical emissions underestimated.

Likewise, the GOSAT-based inversion results indicate *a posteriori* emissions increases from the *a priori* emissions are centred around tropical regions. In 2020, there are emissions increases from the *a priori* estimates in Tropical South America ( $+20.3 \pm 1.9$  Tg/yr) and North Africa ( $+13.1 \pm 6.8$  Tg/yr). Similar to the *in situ* results, there are decreases in some mid-  
260 latitudinal regions, specifically Temperate North America ( $-3.9 \pm 1.8$  Tg/yr) and Temperate South America ( $-6.4 \pm 7.1$  Tg/yr).

The increase in tropical emissions has been highlighted by previous studies, whether using GOSAT data or *in situ* data as constraints in a 3-D CTM inversion (McNorton et al., 2016 and Fujita et al., 2020, examining (2003-2015) and (1995-2013) respectively). The increase in North Africa is especially noteworthy in 2020, where emissions have been attributed to increased wet-land emissions by previous studies (~~Lunt et al., 2019, 2021; Pandey et al., 2021; Feng et al., 2022b~~ Lunt et al., 2019, 2021; Pandey et al., 20  
265 ).

There are some differences between the two inversion results, likely due to the differing geographic coverage of the different datasets (ground-based data has poorer geographic coverage, and satellite data are available only once per day in cloud-free conditions). Specifically, emissions from Boreal North America and China are lower than the *a priori* emissions for the GOSAT-based inversion ( ~~$-4.6$   $-4.6$~~   $\pm 1.1$  and  ~~$-5.1$   $-5.1$~~   $\pm 3.8$  Tg/yr in 2020 respectively), but increase for the *in situ* inversion ( $+4.4 \pm$   
270  ~~$3$   $-3.6$~~  and  $+17.3 \pm 4.4$  Tg/yr in 2020 respectively). It is noteworthy that, despite differences in the absolute annual emissions estimates, both the GOSAT-based inversion and the *in situ* based inversion indicate a gradual emissions increase in China from 2012. Sheng et al. (2021) find **anthropogenic**  $\text{CH}_4$  emissions from China increasing by 0.36 Tg/yr, from 2012 to 2017 using GOSAT data. Comparing the same time period, we find an increase of Chinese emissions of  ~~$0.72$   $0.63$~~  Tg/yr inferred from the ground-based *in situ* data and increase of  ~~$1.34$   $0.50$~~  Tg/yr inferred from the GOSAT data. We find that China has an isotopically lighter  $\delta^{13}\text{C}$  source signature from 2012 (Figure 4), similar to the other regions we study, however the isotopic shift in the latitude band that corresponds to China is not as large as in others (Figure A), which suggests that heavier isotopic signature sources (such as coal mines) could be part of the emissions makeup here.

~~Figure~~ We see improved emissions estimates for *a posteriori* versus *a priori* simulations. Figure A1 shows mole fraction estimates and *a posteriori* mole fraction estimates inferred from ~~the NOAA surface ground-based~~ data at site locations. We  
280 find smaller residuals between simulated mole fractions using the *a posteriori* emissions and the measurements (mean residual 9.01 ppb; root-mean-square error (RMSE) 11.94 ppb) than between the *a priori* values and the measurements (mean residual 13.06 ppb; RMSE 17.13 ppb). This compares favourably with studies such as McNorton et al. (2018), with *a posteriori* RMSE of 12.30 ppb. Likewise, we see agreement of mole fraction estimates using GOSAT data (Figure A2; mean residual 41.72 ppb, RMSE 51.57 ppb). There are no significant *a posteriori* correlations between neighbouring regions (Figure A3), determined

285 by the *a posteriori* error covariance matrix, **A**, meaning that the *a posteriori* regional emissions estimates are independent of one another.

Figure A4 shows the monthly regional source signature values for Independent validation of the *a priori* *a posteriori* simulations. General observations from this figure are that lighter signatures are observed ( $-62\%$ ) from Northern Boreal regions (Boreal North America and Eurasia), which indicates the dominance of biogenic emissions here. Conversely, we observe heavier source signatures ( $-40\%$ , indicative of a greater proportion of anthropogenic emissions) from regions such as Temperate Eurasia, Australia and Southern Africa. Some regional  $\delta^{13}\text{C}$  source signatures have a much stronger seasonal cycle than others (strongest in Boreal North America and Boreal Eurasia but also in Northern and Southern Africa), with lighter values during summer months, driven by a greater proportion of biogenic emissions at this time. It therefore follows that less significant seasonality is indicative of anthropogenic emissions making up a significant part of the emissions mix (observed for example in China and Temperate Eurasia). Tropical Asia shows a yearly cycle with dual peaks, which is due to a combination of wetland and rice emissions. This assessment assumes that sources are playing the most significant role in controlling seasonal cycle in  $\delta^{13}\text{C}$  source signature, although we do not discount a role for changes in the loss processes mole fractions are provided by comparison with NOAA network sites not included in the inversion (Figure A7).

Figure 4 shows *a posteriori* regional  $\delta^{13}\text{C}$  emissions source signatures inferred from ground-based *in situ* data. The results are grouped into approximately three-year bands, as a residual from the 2004-2007 mean value, to show how the regional isotopic source signatures change across the time series. There is a Relative to *a priori* emissions (Figure A4), *a posteriori* values from Northern Boreal regions (Boreal North America and Eurasia) have isotopically lighter signatures ( $-62\%$ ), consistent with the dominance of biogenic emissions (Figure A4). Conversely, *a posteriori* values from regions such as Temperate Eurasia, Australia and Southern Africa have isotopically heavier source signatures (approximately  $-40\%$ ), suggesting a greater proportion of thermogenic or pyrogenic emissions. Figure 4 shows a general trend towards isotopically lighter regional source signatures of  $\delta^{13}\text{C}$  across the time series. This trend has been ongoing since 2012 and is observed in all regions worldwide, however is strongest as compared with *a priori* estimates in Tropical and Southern Hemispheric regions such as Tropical South America and Southern Africa ( $1.8\%$  and  $2.1\%$  isotopically lighter than *a priori* for 2019-2020 2019 and 2020, respectively). Emissions from these tropical regions have a strong  $\delta^{13}\text{C}$  seasonal cycle (Figure A4), with isotopically lighter values during summer months, driven by a greater proportion of biogenic emissions at this time. It therefore follows that less significant seasonality is indicative of thermogenic or pyrogenic emissions making up a significant part of the emissions mix (observed for example in China and Temperate Eurasia). There is also evidence to suggest a period around 2012 when regional source signatures become isotopically heavier (by approximately  $1.0\%$  compared with *a priori* source signatures), especially in the Northern Hemisphere, before becoming isotopically lighter again. The heavy trend is dominant in the Northern Hemisphere, suggesting a larger proportion of anthropogenic emissions in this region at this time. This heavy shift around This suggests a change in the sources of  $\text{CH}_4$  dominating  $\text{CH}_4$  emissions during this brief period. These isotopic shifts in 2008 and light shift in 2012 is also are noted by Nisbet et al. (2016), who use a box model and examine data from sites measured by NOAA and Royal Holloway, University of London (RHUL). They found that changes in removal rates would not explain these anomalies;

the events are therefore attributed to changing emissions. ~~Emissions growth post-2012 aligns with our atmospheric growth rates plotted in Figures 6, 3.~~

We find some significant *a posteriori* correlations between neighbouring regions for these source signatures (Figure A5), determined by the *a posteriori* error covariance matrix, **A**, which indicates that we cannot differentiate between the isotopic source signatures of neighbouring regions (such as Southern Africa and Temperate South America). This aligns with Basu et al. (2022), who used both CH<sub>4</sub> mole fraction and  $\delta^{13}\text{C}$  measurements to determine that tropical biogenic sources are driving CH<sub>4</sub> growth,  
325 however acknowledge that measurement coverage limits possible conclusions based upon isotope ratio measurements. Nevertheless, the trend of stronger emissions of isotopically lighter CH<sub>4</sub> is clear, indicating an increased role in biogenic ~~or wetland~~ emissions in the global source makeup. ~~Lan et al. (2021) corroborate this using a 3-D chemical transport model to simulate different possible emissions scenarios, and find that microbial emissions (wetlands, agriculture and waste) are responsible for increasingly light  $\delta^{13}\text{C}$  signature, examining 1984-2016.~~

330 The corresponding *a posteriori* regional  $\delta^{13}\text{C}$  source signatures produce an atmospheric time series more consistent with measurements than *a priori* values (Figure A6), particularly during 2008-2018 when *a priori* ~~values result in significantly lighter~~ emissions source signatures. ~~Figure are significantly isotopically lighter.~~ Figure A6 shows  $\delta^{13}\text{C}$  *a priori* and *a posteriori* values at site locations. The *a posteriori* source signatures result in smaller residuals between the *a posteriori* simulation and ~~measurement measurements~~ (mean residual 0.11‰, RMSE 0.15‰), than from the prior (mean residual 0.19‰, RMSE  
335 0.23‰). ~~These compare~~ This result compares well to McNorton et al. (2018) (*a posteriori* RMSE 0.1‰) and Fujita et al. (2020) (*a posteriori* RMSE 0.08–~~0.25–0.25~~‰).

In Figure A, we combine this information into a zonal plot, reported approximately every 30° latitude, for CH<sub>4</sub> emissions and the corresponding changes in regional isotopic source signatures of  $\delta^{13}\text{C}$ . We find consistency between the magnitude of the changes in CH<sub>4</sub> inferred from NOAA ground-based and GOSAT data, particularly in the low latitudes. The plot also shows  
340 there has been a progressive increase in emissions from tropical latitudes (between 60-80 Tg/yr in 2019-2020) and a decrease at northern midlatitudes (up to -10 Tg/yr). This suggests that emissions have shifted from northern midlatitudes towards tropical emissions. We also find a move towards isotopically lighter regional source signatures of  $\delta^{13}\text{C}$  across all latitudinal bands, with a change of approximately -2‰ in the tropics. Comparing Figures 4 and A, we see similar trends across latitudinal bands and the regions within them, for example trends in European and Chinese source signatures align with the 30-60°N latitudinal band.  
345 Our results compare well with Nisbet et al. (2019), who use a box model to fit emissions scenarios to *in situ* measurements, examining 2000-2018. They show strongest emissions increases from the tropics (approximately +20 Tg/yr, Figure 5). They likewise show consistently lighter isotopically lighter atmospheric  $\delta^{13}\text{C}$  ~~across the time series of  $\delta^{13}\text{C}$  by approximately 0.5,~~  
by approximately 0.03‰/yr.

Figure 6 compares our calculated atmospheric growth rate from the model simulations with the growth rates calculated from  
350 the *in situ* observations alone. We applied the same technique as NOAA follow to compare their published growth rate to the *a posteriori* mole fractions of our inversion. The general trend in increasing growth rate is evident in both measurement and model datasets with inter-annual discrepancies explained through model measurement mismatch at specific sites.

To examine the sensitivity of our results to changes in OH, we run a single sensitivity run that is made up of two parts. First, we imposed a 0.5 %/yr uniform decrease to our 3-D OH field from 2004 to 2019, following similar trends proposed by Turner et al. (2017) (who proposed a 7 % reduction in OH, 2003-2016) and second, we uniformly decrease OH by 5 % in 2020 to describe estimated changes due to a global-scale reduction in emissions of nitrogen oxides ( $\text{NO}_x$ ) associated with the first COVID-19 lockdown Miyazaki et al. (2021); Laughner et al. (2021). It has also been suggested that OH levels may have actually increased during 2000–2016 due to increasing water vapour and  $\text{NO}_x$  in the tropics (Zhao et al., 2019), however considering the scenario under COVID-19 lockdowns in 2020, a decreasing trend over the previous years is only considered here. A similar approach to this was followed by Feng et al. (2022b) for which there is some opposition that suggests the change in OH during COVID-19 should be larger although there is no empirical determination of this change. We then recalculate *a posteriori* emissions inferred from the in situ NOAA data. Figure 7 shows that the 0.5% negative trend in OH does not make a significant difference to our *a posteriori* estimates (emissions change is not larger than *a posteriori* uncertainty) until later in the timeseries (2017-2019), reflecting our large *a posteriori* uncertainties. However, we find that a sudden 5% decrease in OH during 2020 results in a marked reduction (approximately 9%, 50 Tg/yr) in the increased emissions necessary to explain the increase in atmospheric  $\text{CH}_4$ . This reduction in necessary increases in emissions particularly affects high-emitting regions such as China and Tropical Asia. Despite this, the regional results are generally within the *a posteriori* uncertainties of our control calculation, which does not include a year-to-year change in OH. On balance, given the large-scale, unprecedented changes in atmospheric chemistry during 2020 it is likely that OH has a role to play in the global atmospheric growth rate of  $\text{CH}_4$ , but changes in emissions likely overwhelm the impact from reduced OH. We find a similar fit of the model to data with or without considering the OH trend (not shown).

#### 4 Conclusions

We estimated regional  $\text{CH}_4$  emissions and  $\delta^{13}\text{C}$  source signatures for the period 2004-2020, inclusively, by fitting the GEOS-Chem 3-D atmospheric chemistry transport model to NOAA in situ surface mole fraction data and GOSAT atmospheric column data using Bayesian inverse methods. Collectively, our results indicate that the post-2007 increase in  $\text{CH}_4$  emissions are best explained by a progressive latitudinal shift in emissions from the northern midlatitudes to tropical latitudes. *A posteriori*  $\text{CH}_4$  emission estimates inferred from the NOAA ground-based and GOSAT data show larger tropical emissions, particularly over North Africa, Tropical Asia, and Tropical South America, at the same time as mid-latitudinal emission proportion decreases. Source signature estimates inferred from the  $\delta^{13}\text{C}$  measurements over the same time period indicate that the latitudinal shift in  $\text{CH}_4$  emissions is due to larger proportion of biogenic sources. Our results are broadly consistent with previous studies that focus on shorter, contributing periods (McNorton et al., 2018; Nisbet et al., 2019; Fujita et al., 2020; Yin et al., 2021; Lan et al., 2021) (McNorton et al., 2018; Nisbet et al., 2019; Fujita et al., 2020; Yin et al., 2021; Lan et al., 2021; Basu et al., 2022)).

Our control calculations used monthly 3-D distributions of OH without any year-to-year variation. To explore how changes in OH might affect our results, we ran a sensitivity experiment for which the monthly 3-D OH fields was decreased 0.5%/yr from 2004 to 2019, inclusively, based on values proposed by previous studies (Turner et al., 2017). For this sensitivity experiment,

we find our results are within *a posteriori* uncertainty of the control calculations for most of the time series, and therefore steadily decreasing OH concentrations are not responsible for observed changes in the distribution of CH<sub>4</sub>. We also considered how a proposed larger 5% change in 2020 (Miyazaki et al., 2021; Laughner et al., 2021), due to widespread COVID-19 related emission reductions in nitrogen oxides, affected our results. We find smaller CH<sub>4</sub> emissions increases during 2020, as expected, but for most regions they are still within our control *a posteriori* emissions estimates for 2020. A much larger reduction in OH would be necessary to describe exclusively observed changes in atmospheric CH<sub>4</sub>, which would consequently affect regional isotope signatures and observed variations of many atmospheric trace gases in a manner that has yet to be reported.

Sparse geographic coverage of ground-based data results in larger uncertainties for regional emission estimates that are poorly covered, i.e., high and low latitudes. For CH<sub>4</sub>, this deficiency can be partly addressed using the satellite data, but ~~isotopes are not currently retrieved reliably from satellite remote sensing~~ isotope ratios cannot usefully be retrieved from Earth observation satellite instruments. In this study, ~~there are only three long-term~~ We use only three measurement sites for  $\delta^{13}\text{C}$  ~~employed in the southern hemisphere~~ in the Southern Hemisphere, which have a continuous record over the period of study. A consequence of this data sparseness is strong correlations between source signatures from neighbouring regions (Figure A5). We further limited our study by picking measurements sites for which data are available over our study period (Figure 1). Sectoral ~~source signatures~~  $\delta^{13}\text{C}$  source signatures are taken as mean values from Sherwood et al. (2017), ~~representing our current best knowledge. Different~~ These values are highly uncertain, as different sectors produce a range of possible  $\delta^{13}\text{C}$  values, and there are significant overlaps between recorded source signatures (Douglas et al., 2017), ~~but the values chosen represent our current best knowledge of mean values~~. These data have greater value when they are used in a broader context with other data, as we have described in this study. We have used satellite observations to help identify that large-scale emission changes over regions that coincide with wetlands. The collective evidence demonstrates that increasing ~~natural, tropical~~ tropical wetland emissions play a significant role in the observed atmospheric growth of CH<sub>4</sub>. Greater confidence in source attribution of changes in atmospheric CH<sub>4</sub> may come from collecting and interpreting  $\delta\text{D}$  and multiply-substituted ‘clumped’ isotopes (~~Douglas et al., 2017~~) (Douglas et al., 2017; Chung and Arnold, 2021), alongside  $\delta^{13}\text{C}$ . This needs to be accompanied by ~~laboratory and~~ field measurements of these ~~isotopes~~ isotope ratios to improve delineation between different sectors.

Our work is also consistent with recent studies that have reported anomalous large CH<sub>4</sub> emissions over Eastern Africa (East Africa and the Horn of Africa) due to elevated rainfall over upstream catchment areas (Lunt et al., 2019, 2021; Pandey et al., 2021). These large-scale precipitation changes have been linked with the positive phase of the Indian Ocean Dipole (~~Feng et al., 2022b~~) (Feng et al., 2022b), which describes a sea-surface temperature gradient over the Indian Ocean. Similarly, ~~increase~~ increased CH<sub>4</sub> emissions over the Amazon basin (Wilson et al., 2021) are linked with large-scale changes in climate (~~Feng et al., 2022b~~) (Feng et al., 2022b). These substantial increases in ~~natural~~ biogenic CH<sub>4</sub> emissions will likely have major implications for our achieving the goals of the Paris Agreement (Nisbet et al., 2019). Nature does not care about the origin of atmospheric CH<sub>4</sub> so that increasing ~~natural~~ biogenic emissions will require larger emission reductions from anthropogenic sectors, placing additional pressure on citizens to reduce their carbon footprints.

## 5 Code and data availability

420 The community-led GEOS-Chem model of atmospheric chemistry and model is maintained centrally by Harvard University (<http://geos-chem.seas.harvard.edu>), and is available on request. The ensemble Kalman filter code is publicly available as PyOSSE (<https://www.nceo.ac.uk/data-tools/atmospheric-tools/>).

All the data and materials used in this study are freely available. The NOAA-GML and CU-INSTAAR ground-based CH<sub>4</sub> and δ<sup>13</sup>C data are available from the NOAA GML FTP server (<https://gml.noaa.gov/dv/data>), subject to their fair use policies.

425 Data from JR-STATION network was provided with cooperation of NIES Japan. The University of Leicester GOSAT Proxy v9.0 XCH<sub>4</sub> data are available from the Centre for Environmental Data Analysis data repository at (<https://doi.org/10.5285/18ef8247f52a4cb6a14013f8235cc1eb>), and from the Copernicus Climate Data Store. EDGAR data is available at (<https://edgar.jrc.ec.europa.eu/>), GFED-4 data is available at (<https://www.globalfiredata.org/data.html>), WETCHARTS data is available at ([https://daac.ornl.gov/cgi-bin/dsviewer.pl?ds\\_id=1502](https://daac.ornl.gov/cgi-bin/dsviewer.pl?ds_id=1502)).

### 430 Appendix A: Isotopologue Emissions

To simulate the atmospheric isotope ratio δ<sup>13</sup>C the isotopologues <sup>12</sup>CH<sub>4</sub> and <sup>13</sup>CH<sub>4</sub> are considered separately in the model. To calculate the specific sectoral isotopologue emissions we use the emissions calculated from the ~~total-mole fraction~~ CH<sub>4</sub> simulation and the isotope ratios defined in Table 1. We consider the isotope ~~<sup>13</sup>C-<sup>13</sup>C~~ relative to all isotopes in the sample (designated thereafter as ~~<sup>13</sup>x<sup>13</sup>x~~) using:

$$435 \quad 13x = \frac{{}^{13}\text{C}}{{}^{12}\text{C} + {}^{13}\text{C}} = \frac{{}^{13}\text{C}/{}^{12}\text{C}}{1 + ({}^{13}\text{C}/{}^{12}\text{C})}, \quad (\text{A1})$$

where ~~<sup>13</sup>C/<sup>12</sup>C~~ <sup><sup>13</sup>C/<sup>12</sup>C</sup> is calculated from the δ<sup>13</sup>C reported on the international carbon isotope scale (~~VPDB-VPDB~~ Vienna Pee Dee Belemnite). This is the proportional molar abundance of the isotopologues containing ~~<sup>13</sup>C-<sup>13</sup>C~~ (dominated by <sup>13</sup>CH<sub>4</sub>) relative to the isotopologues containing <sup>12</sup>C (dominated by <sup>12</sup>CH<sub>4</sub>). This value has to be adjusted before being applied in GEOS-Chem to convert from isotope ratio values to kg values used by emission inventories:

$$440 \quad SF13 = 13x \times \frac{M_{13}}{M_{tot}}, \quad (\text{A2})$$

where ~~SF13~~ SF13 is the scale factor applied to each emissions type for the <sup>13</sup>CH<sub>4</sub> simulation,  $M_{13}$  is the molecular weight of <sup>13</sup>CH<sub>4</sub> (17.035 g/mol) and  $M_{tot}$  is the molecular weight of CH<sub>4</sub> (16.04 g/mol).

For the <sup>12</sup>CH<sub>4</sub> counterpart to <sup>13</sup>CH<sub>4</sub>, we use a similar approach. The ratio of ~~<sup>12</sup>C-<sup>12</sup>C~~ compared with all isotopes in the sample (designated as ~~<sup>12</sup>x<sup>12</sup>x~~) is given by:

$$445 \quad 12x = \frac{{}^{12}\text{C}}{{}^{13}\text{C} + {}^{12}\text{C}}. \quad (\text{A3})$$



This is similarly adjusted from molar to mass ratio; ~~'SF12'~~  $SF_{12}$  is the scale factor for each emissions type in the  $^{12}\text{CH}_4$  simulations:

$$SF_{12} = 12x \times \frac{M_{12}}{M_{tot}}, \quad (\text{A4})$$

where  $M_{12}$  is the molecular weight of  $^{12}\text{CH}_4$  (16.03 g/mol). Since  ~~$^{13}\text{C}$  and  $^{12}\text{C}$~~   $^{13}\text{C}$  and  $^{12}\text{C}$  are the only stable carbon isotopes of  $\text{CH}_4$ ,  ~~$^{13}\text{C}$  and  $^{12}\text{C}$~~   $^{13}\text{C}$  and  $^{12}\text{C}$  should sum to 1.

*Author contributions.* A.D. led the data analysis with contributions from P.I.P. and L.F. A.D. led the writing of the paper with contributions from P.I.P., L.F., T.A., X.L., S.M., R.P. and H.M. provided data.

*Competing interests.* The authors declare that they have no competing interests.

*Acknowledgements.* A.D. is supported by the University of Edinburgh's E3 Doctoral Training Partnership, funded by the National Environment Research Council. P.I.P., L.F. and R.P. acknowledge support from the UK National Centre for Earth Observation funded by the National Environment Research Council (NE/R016518/1 and NE/N018079/1) and the Copernicus Climate Change Service (C3S2\_312a\_Lot2). This work is also supported through a contribution by the National Physical Laboratory, UK to the studentship. We thank NOAA ESRL and CU-INSTAAR for providing  $\text{CH}_4$  and  $\delta^{13}\text{C}$  data. We thank the Japanese National Institute for Environmental Studies and the Ministry of Environment for the GOSAT data and their continuous support as part of the Joint Research Agreements at the Universities of Edinburgh and Leicester. We also thank the GEOS-Chem community, particularly the team at Harvard who help maintain the GEOS-Chem model, and the NASA Global Modeling and Assimilation Office (GMAO) who provide the MERRA-2 data product.

## References

- Basu, S., Lan, X., Dlugokencky, E., Michel, S., Schwietzke, S., Miller, J. B., Bruhwiler, L., Oh, Y., Tans, P. P., Apadula, F., Gatti, L. V., Jordan, A., Necki, J., Sasakawa, M., Morimoto, S., Di Iorio, T., Lee, H., Arduini, J., and Manca, G.: Estimating Emissions of Methane Consistent with Atmospheric Measurements of Methane and  $\delta^{13}\text{C}$  of Methane, *Atmospheric Chemistry and Physics Discussions*, 2022, 1–38, <https://doi.org/10.5194/acp-2022-317>, 2022.
- Bey, I., Jacob, D. J., Yantosca, R. M., Logan, J. A., Field, B. D., Fiore, A. M., Li, Q., Liu, H. Y., Mickley, L. J., and Schultz, M. G.: Global modeling of tropospheric chemistry with assimilated meteorology: Model description and evaluation, *Journal of Geophysical Research Atmospheres*, 106, 23 073–23 095, <https://doi.org/10.1029/2001JD000807>, 2001.
- Bloom, A. A., Bowman, K. W., Lee, M., Turner, A. J., Schroeder, R., Worden, J. R., Weidner, R., McDonald, K. C., and Jacob, D. J.: A global wetland methane emissions and uncertainty dataset for atmospheric chemical transport models (WetCHARTs version 1.0), *Geosci. Model Dev.*, 10, 2141–2156, <https://doi.org/10.5194/gmd-10-2141-2017>, 2017.
- Burkholder, J. B., Sander, S. P., Abbatt, J., Barker, J. R., Cappa, C., Crouse, J. D., Dibble, T. S. and Huie, R. E., Kolb, C. E., Kurylo, M. J., Orkin, V. L., Percival, C. J., Wilmouth, D. M., and Wine, P. H.: Chemical Kinetics and Photochemical Data for Use in Atmospheric Studies, Evaluation No. 19, Tech. rep., JPL Publication 19-5, Jet Propulsion Laboratory, Pasadena, 2019.
- Chung, E. and Arnold, T.: Potential of Clumped Isotopes in Constraining the Global Atmospheric Methane Budget, *Global Biogeochemical Cycles*, 35, e2020GB006 883, <https://doi.org/10.1029/2020GB006883>, e2020GB006883 2020GB006883, 2021.
- Dlugokencky, E., Crotwell, A., Mund, J., and Thoning, K.: Atmospheric Methane Dry Air Mole Fractions from the NOAA GML Carbon Cycle Cooperative Global Air Sampling Network, 1983–2019, Version: 2020-07, <https://doi.org/https://doi.org/10.15138/VNCZ-M766>, 2020.
- Dlugokencky, E. J., Myers, R. C., Lang, P. M., Masarie, K. A., Crotwell, A. M., Thoning, K. W., Hall, B. D., Elkins, J. W., and Steele, L. P.: Conversion of NOAA atmospheric dry air CH<sub>4</sub> mole fractions to a gravimetrically prepared standard scale, *Journal of Geophysical Research: Atmospheres*, 110, <https://doi.org/10.1029/2005JD006035>, 2005.
- Dlugokencky, E., Steele, L., Lang, P., and Masarie, K.: The growth rate and distribution of atmospheric methane, *Journal of Geophysical Research: Atmospheres*, 99, 17 021–17 043, <https://doi.org/https://doi.org/10.1029/94JD01245>, 1994.
- Douglas, P. M., Stolper, D. A., Eiler, J. M., Sessions, A. L., Lawson, M., Shuai, Y., Bishop, A., Podlaha, O. G., Ferreira, A. A., Santos Neto, E. V., Niemann, M., Steen, A. S., Huang, L., Chimiak, L., Valentine, D. L., Fiebig, J., Luhmann, A. J., Seyfried, W. E., Etiope, G., Schoell, M., Inskeep, W. P., Moran, J. J., and Kitchen, N.: Methane clumped isotopes: Progress and potential for a new isotopic tracer, *Organic Geochemistry*, 113, 262–282, <https://doi.org/10.1016/j.orggeochem.2017.07.016>, 2017.
- Duncan, B. N., Strahan, S. E., Yoshida, Y., Steenrod, S. D., and Livesey, N.: Model study of the cross-tropopause transport of biomass burning pollution, *Atmospheric Chemistry and Physics*, 7, 3713–3736, <https://doi.org/10.5194/acp-7-3713-2007>, 2007.
- Feilberg, K. L., Griffith, D. W. T., Johnson, M. S., and Nielsen, C. J.: The <sup>13</sup>C and D kinetic isotope effects in the reaction of CH<sub>4</sub> with Cl, *International Journal of Chemical Kinetics*, 37, 110–118, <https://doi.org/https://doi.org/10.1002/kin.20058>, 2005.
- Feng, L., Palmer, P. I., Bösch, H., Parker, R. J., Webb, A. J., Correia, C. S. C., Deutscher, N. M., Domingues, L. G., Feist, D. G., Gatti, L. V., Gloor, E., Hase, F., Kivi, R., Liu, Y., Miller, J. B., Morino, I., Sussmann, R., Strong, K., Uchino, O., Wang, J., and Zahn, A.: Consistent regional fluxes of CH<sub>4</sub> and CO<sub>2</sub> inferred from GOSAT proxy XCH<sub>4</sub> : XCO<sub>2</sub> retrievals, 2010–2014, *Atmospheric Chemistry and Physics*, 17, 4781–4797, <https://doi.org/10.5194/acp-17-4781-2017>, 2017.

- Feng, L., Palmer, P. I., Parker, R. J., Lunt, M. F., and Boesch, H.: Methane emissions responsible for record-breaking atmospheric methane growth rates in 2020 and 2021, *Atmospheric Chemistry and Physics Discussions*, 2022, 1–23, <https://doi.org/10.5194/acp-2022-425>, 2022a.
- 500
- Feng, L., Palmer, P. I., Zhu, S., Parker, R. J., and Liu, Y.: Tropical methane emissions explain large fraction of recent changes in global atmospheric methane growth rate, *Nature Communications*, 13, 1378, <https://doi.org/10.1038/s41467-022-28989-z>, 2022b.
- Fraser, A., Palmer, P. I., Feng, L., Bösch, H., Parker, R., Dlugokencky, E. J., Krummel, P. B., and Langenfelds, R. L.: Estimating regional fluxes of CO<sub>2</sub> and CH<sub>4</sub> using space-borne observations of XCH<sub>2</sub>: XCO<sub>2</sub>, *Atmospheric Chemistry and Physics*, 14, 12 883–12 895, <https://doi.org/10.5194/acp-14-12883-2014>, 2014.
- 505
- Fujita, R., Morimoto, S., Maksyutov, S., Kim, H.-S., Arshinov, M., Brailsford, G., Aoki, S., and Nakazawa, T.: Global and Regional CH<sub>4</sub> Emissions for 1995–2013 Derived From Atmospheric CH<sub>4</sub>,  $\delta^{13}\text{C-CH}_4$ , and  $\delta\text{D-CH}_4$  Observations and a Chemical Transport Model, *Journal of Geophysical Research: Atmospheres*, 125, e2020JD032 903, <https://doi.org/https://doi.org/10.1029/2020JD032903>, e2020JD032903 2020JD032903, 2020.
- 510
- Fung, I., John, J., Lerner, J., Matthews, E., Prather, M., Steele, L. P., and Fraser, P. J.: <Three-dimensional model synthesis of the global methane cycle-Fung 1991.pdf>, *JOURNAL OF GEOPHYSICAL RESEARCH*, 96, 33–46, [https://pubs.giss.nasa.gov/docs/1991/1991\\_{\\_}Fung\\_{\\_}fu08000d.pdf](https://pubs.giss.nasa.gov/docs/1991/1991_{_}Fung_{_}fu08000d.pdf), 1991.
- Ganesan, A. L., Stell, A. C., Gedney, N., Comyn-Platt, E., Hayman, G., Rigby, M., Poulter, B., and Hornibrook, E. R. C.: Spatially Resolved Isotopic Source Signatures of Wetland Methane Emissions, *Geophysical Research Letters*, 45, 3737–3745, <https://doi.org/10.1002/2018GL077536>, 2018.
- 515
- Gelaro, R., McCarty, W., Suárez, M. J., Todling, R., Molod, A., Takacs, L., Randles, C. A., Darmenov, A., Bosilovich, M. G., Reichle, R., Wargan, K., Coy, L., Cullather, R., Draper, C., Akella, S., Buchard, V., Conaty, A., da Silva, A. M., Gu, W., Kim, G. K., Koster, R., Lucchesi, R., Merkova, D., Nielsen, J. E., Partyka, G., Pawson, S., Putman, W., Rienecker, M., Schubert, S. D., Sienkiewicz, M., and Zhao, B.: The modern-era retrospective analysis for research and applications, version 2 (MERRA-2), *Journal of Climate*, 30, 5419–5454, <https://doi.org/10.1175/JCLI-D-16-0758.1>, 2017.
- 520
- Gurney, K. R., Law, R. M., Denning, A. S., Rayner, P. J., Baker, D., Bousquet, P., Bruhwiler, L., Chen, Y.-H., Ciais, P., Fan, S., Fung, I. Y., Gloor, M., Heimann, M., Higuchi, K., John, J., Maki, T., Maksyutov, S., Masarie, K., Peylin, P., Prather, M., Pak, B. C., Randerson, J., Sarmiento, J., Taguchi, S., Takahashi, T., and Yuen, C.-W.: Towards robust regional estimates of CO<sub>2</sub> sources and sinks using atmospheric transport models, *Nature*, 415, 626–630, <https://doi.org/10.1038/415626a>, 2002.
- 525
- Janssens-Maenhout, G., Crippa, M., Guizzardi, D., Muntean, M., Schaaf, E., Dentener, F., Bergamaschi, P., Pagliari, V., Olivier, J. G. J., Peters, J. A. H. W., van Aardenne, J. A., Monni, S., Doering, U., Petrescu, A. M. R., Solazzo, E., and Oreggioni, G. D.: EDGAR v4.3.2 Global Atlas of the three major greenhouse gas emissions for the period 1970–2012, *Earth System Science Data*, 11, 959–1002, <https://doi.org/10.5194/essd-11-959-2019>, 2019.
- Kirschke, S., Bousquet, P., Ciais, P., Saunoy, M., Canadell, J. G., Dlugokencky, E. J., Bergamaschi, P., Bergmann, D., Blake, D. R., Bruhwiler, L., Cameron-Smith, P., Castaldi, S., Chevallier, F., Feng, L., Fraser, A., Heimann, M., Hodson, E. L., Houweling, S., Josse, B., Fraser, P. J., Krummel, P. B., Lamarque, J. F., Langenfelds, R. L., Le Quééré, C., Naik, V., O’doherly, S., Palmer, P. I., Pison, I., Plummer, D., Poulter, B., Prinn, R. G., Rigby, M., Ringeval, B., Santini, M., Schmidt, M., Shindell, D. T., Simpson, I. J., Spahni, R., Steele, L. P., Strode, S. A., Sudo, K., Szopa, S., Van Der Werf, G. R., Voulgarakis, A., Van Weele, M., Weiss, R. F., Williams, J. E., and Zeng, G.: Three decades of global methane sources and sinks, <https://doi.org/10.1038/ngeo1955>, 2013.
- 530

- 535 Lan, X., Basu, S., Schwietzke, S., Bruhwiler, L. M. P., Dlugokencky, E. J., Michel, S. E., Sherwood, O. A., Tans, P. P., Thoning, K., Etiope, G., Zhuang, Q., Liu, L., Oh, Y., Miller, J. B., Pétron, G., Vaughn, B. H., and Crippa, M.: Improved Constraints on Global Methane Emissions and Sinks Using  $\delta^{13}\text{C}\text{-CH}_4$ , *Global Biogeochemical Cycles*, 35, e2021GB007000, <https://doi.org/https://doi.org/10.1029/2021GB007000>, e2021GB007000 2021GB007000, 2021.
- Laughner, J. L., Neu, J. L., Schimel, D., Wennberg, P. O., Barsanti, K., Bowman, K. W., Chatterjee, A., Croes, B. E., Fitzmaurice, H. L.,  
540 Henze, D. K., Kim, J., Kort, E. A., Liu, Z., Miyazaki, K., Turner, A. J., Anenberg, S., Avise, J., Cao, H., Crisp, D., de Gouw, J., Eldering, A., Fyfe, J. C., Goldberg, D. L., Gurney, K. R., Hasheminassab, S., Hopkins, F., Ivey, C. E., Jones, D. B. A., Liu, J., Lovenduski, N. S., Martin, R. V., McKinley, G. A., Ott, L., Poulter, B., Ru, M., Sander, S. P., Swart, N., Yung, Y. L., and Zeng, Z.-C.: Societal shifts due to COVID-19 reveal large-scale complexities and feedbacks between atmospheric chemistry and climate change, *Proceedings of the National Academy of Sciences*, 118, <https://doi.org/10.1073/pnas.2109481118>, 2021.
- 545 Lunt, M. F., Palmer, P. I., Feng, L., Taylor, C. M., Boesch, H., and Parker, R. J.: An increase in methane emissions from tropical Africa between 2010 and 2016 inferred from satellite data, *Atmospheric Chemistry and Physics*, 19, 14 721–14 740, <https://doi.org/10.5194/acp-19-14721-2019>, 2019.
- Lunt, M. F., Palmer, P. I., Lorente, A., Borsdorff, T., Landgraf, J., Parker, R. J., and Boesch, H.: Rain-fed pulses of methane from East Africa during 2018–2019 contributed to atmospheric growth rate, *Environmental Research Letters*, 16, 024 021, <https://doi.org/10.1088/1748-9326/abd8fa>, 2021.  
550
- Masson-Delmotte, V., Zhai, P., A. Pirani, S. C., C. Péan, S. B., Caud, N., Chen, Y., Gomis, L. G. M., Huang, M., Leitzell, K., Lonnoy, E., Matthews, J., Maycock, T., Waterfield, T., Yelekçi, O., Yu, R., and Zhou, B.: *Climate Change 2021: The Physical Science Basis. Contribution of Working Group I to the Sixth Assessment Report of the Intergovernmental Panel on Climate Changes*, Tech. rep., IPCC, WMO Geneva, 2021.
- 555 McNorton, J., Chipperfield, M. P., Gloor, M., Wilson, C., Feng, W., Hayman, G. D., Rigby, M., Krummel, P. B., O’Doherty, S., Prinn, R. G., Weiss, R. F., Young, D., Dlugokencky, E., and Montzka, S. A.: Role of OH variability in the stalling of the global atmospheric  $\text{CH}_4$  growth rate from 1999 to 2006, *Atmospheric Chemistry and Physics*, 16, 7943–7956, <https://doi.org/10.5194/acp-16-7943-2016>, 2016.
- McNorton, J., Wilson, C., Gloor, M., Parker, R., Boesch, H., Feng, W., and Chipperfield, M.: Attribution of recent increases in atmospheric methane through 3-D inverse modelling, *Atmos. Chem. Phys.*, 18, 1–34, <https://doi.org/10.5194/acp-2018-474>, 2018.
- 560 Miller, J. B.: Development of analytical methods and measurements of  $^{13}\text{C}/^{12}\text{C}$  in atmospheric  $\text{CH}_4$  from the NOAA Climate Monitoring and Diagnostics Laboratory Global Air Sampling Network, *Journal of Geophysical Research*, 107, 4178, <https://doi.org/10.1029/2001JD000630>, 2002.
- Miyazaki, K., Bowman, K., Sekiya, T., Takigawa, M., Neu, J. L., Sudo, K., Osterman, G., and Eskes, H.: Global tropospheric ozone responses to reduced  $\text{NO}_x$  emissions linked to the COVID-19 worldwide lockdowns, *Science Advances*, 7, eabf7460,  
565 <https://doi.org/10.1126/sciadv.abf7460>, 2021.
- Morgenstern, O., Hegglin, M. I., Rozanov, E., O’Connor, F. M., Abraham, N. L., Akiyoshi, H., Archibald, A. T., Bekki, S., Butchart, N., Chipperfield, M. P., Deushi, M., Dhomse, S. S., Garcia, R. R., Hardiman, S. C., Horowitz, L. W., Jöckel, P., Josse, B., Kinnison, D., Lin, M., Mancini, E., Manyin, M. E., Marchand, M., Marécal, V., Michou, M., Oman, L. D., Pitari, G., Plummer, D. A., Revell, L. E., Saint-Martin, D., Schofield, R., Stenke, A., Stone, K., Sudo, K., Tanaka, T. Y., Tilmes, S., Yamashita, Y., Yoshida, K., and Zeng, G.:  
570 Review of the global models used within phase 1 of the Chemistry–Climate Model Initiative (CCMI), *Geoscientific Model Development*, 10, 639–671, <https://doi.org/10.5194/gmd-10-639-2017>, 2017.

- Nisbet, E. G., Dlugokencky, E. J., Manning, M. R., Lowry, D., Fisher, R. E., France, J. L., Michel, S. E., Miller, J. B., White, J. W., Vaughn, B., Bousquet, P., Pyle, J. A., Warwick, N. J., Cain, M., Brownlow, R., Zazzeri, G., Lanoisellé, M., Manning, A. C., Gloor, E., Worthy, D. E., Brunke, E. G., Labuschagne, C., Wolff, E. W., and Ganesan, A. L.: Rising atmospheric methane: 2007–2014 growth and isotopic shift, *Global Biogeochemical Cycles*, 30, 1356–1370, <https://doi.org/10.1002/2016GB005406>, 2016.
- 575 Nisbet, E. G., Manning, M. R., Dlugokencky, E. J., Fisher, R. E., Lowry, D., Michel, S. E., Myhre, C. L., Platt, S. M., Allen, G., Bousquet, P., Brownlow, R., Cain, M., France, J. L., Hermansen, O., Hossaini, R., Jones, A. E., Levin, I., Manning, A. C., Myhre, G., Pyle, J. A., Vaughn, B. H., Warwick, N. J., and White, J. W. C.: Very Strong Atmospheric Methane Growth in the 4 Years 2014–2017: Implications for the Paris Agreement, *Global Biogeochemical Cycles*, 33, 318–342, <https://doi.org/https://doi.org/10.1029/2018GB006009>, 2019.
- 580 Palmer, P. I., Feng, L., Lunt, M. F., Parker, R. J., Bösch, H., Lan, X., Lorente, A., and Borsdorff, T.: The added value of satellite observations of methane for understanding the contemporary methane budget, *Philosophical Transactions of the Royal Society A: Mathematical, Physical and Engineering Sciences*, 379, 20210 106, <https://doi.org/10.1098/rsta.2021.0106>, 2021.
- Pandey, S., Houweling, S., Lorente, A., Borsdorff, T., Tsvilidou, M., Bloom, A. A., Poulter, B., Zhang, Z., and Aben, I.: Using satellite data to identify the methane emission controls of South Sudan’s wetlands, *Biogeosciences*, 18, 557–572, <https://doi.org/10.5194/bg-18-557-2021>, 585 2021.
- Parker, R., Boesch, H., Cogan, A., Fraser, A., Feng, L., Palmer, P. I., Messerschmidt, J., Deutscher, N., Griffith, D. W. T., Notholt, J., Wennberg, P. O., and Wunch, D.: Methane observations from the Greenhouse Gases Observing SATellite: Comparison to ground-based TCCON data and model calculations, *Geophysical Research Letters*, 38, <https://doi.org/https://doi.org/10.1029/2011GL047871>, 2011.
- Parker, R. J., Boesch, H., Byckling, K., Webb, A. J., Palmer, P. I., Feng, L., Bergamaschi, P., Chevallier, F., Notholt, J., Deutscher, N., 590 Warneke, T., Hase, F., Sussmann, R., Kawakami, S., Kivi, R., Griffith, D. W. T., and Velasco, V.: Assessing 5 years of GOSAT Proxy XCH<sub>4</sub> data and associated uncertainties, *Atmospheric Measurement Techniques*, 8, 4785–4801, <https://doi.org/10.5194/amt-8-4785-2015>, 2015.
- Parker, R. J., Webb, A., Boesch, H., Somkuti, P., Barrio Guillo, R., Di Noia, A., Kalaitzi, N., Anand, J. S., Bergamaschi, P., Chevallier, F., Palmer, P. I., Feng, L., Deutscher, N. M., Feist, D. G., Griffith, D. W. T., Hase, F., Kivi, R., Morino, I., Notholt, J., Oh, Y.-S., 595 Ohyama, H., Petri, C., Pollard, D. F., Roehl, C., Sha, M. K., Shiomi, K., Strong, K., Sussmann, R., Té, Y., Velasco, V. A., Warneke, T., Wennberg, P. O., and Wunch, D.: A decade of GOSAT Proxy satellite CH<sub>4</sub> observations, *Earth System Science Data*, 12, 3383–3412, <https://doi.org/10.5194/essd-12-3383-2020>, 2020.
- Randerson, J., Van Der Werf, G., Giglio, L., Collatz, G., and Kasibhatla, P.: Global Fire Emissions Database, Version 4.1 (GFEDv4), <https://doi.org/10.3334/ORNDAAC/1293>, 2017.
- 600 Rice, A. L., Butenhoff, C. L., Teama, D. G., Röger, F. H., Khalil, M. A. K., and Rasmussen, R. A.: Atmospheric methane isotopic record favors fossil sources flat in 1980s and 1990s with recent increase, *Proceedings of the National Academy of Sciences*, 113, 10 791–10 796, <https://doi.org/10.1073/pnas.1522923113>, 2016.
- Rigby, M., Montzka, S. A., Prinn, R. G., White, J. W. C., Young, D., O’Doherty, S., Lunt, M. F., Ganesan, A. L., Manning, A. J., Simmonds, P. G., Salameh, P. K., Harth, C. M., Mühle, J., Weiss, R. F., Fraser, P. J., Steele, L. P., Krummel, P. B., McCulloch, A., and 605 Park, S.: Role of atmospheric oxidation in recent methane growth, *Proceedings of the National Academy of Sciences*, 114, 5373–5377, <https://doi.org/10.1073/pnas.1616426114>, 2017.
- Rodgers, C. D. C. D.: Inverse methods for atmospheric sounding : theory and practice, Series on atmospheric, oceanic and planetary physics ; vol. 2, World Scientific, Singapore ; London, 2000.

- Sasakawa, M., Shimoyama, K., Machida, T., Tsuda, N., Suto, H., Arshinov, M., Davydov, D., Fofonov, A., Krasnov, O., Saeki, T.,  
610 Koyama, Y., and Maksyutov, S.: Continuous measurements of methane from a tower network over Siberia, *Tellus B*, 62, 403–416,  
<https://doi.org/https://doi.org/10.1111/j.1600-0889.2010.00494.x>, 2010.
- Saunois, M., Bousquet, P., Poulter, B., Peregón, A., Ciais, P., Canadell, J. G., Dlugokencky, E. J., Etiope, G., Bastviken, D., Houweling, S.,  
Janssens-Maenhout, G., Tubiello, F. N., Castaldi, S., Jackson, R. B., Alexe, M., Arora, V. K., Beerling, D. J., Bergamaschi, P., Blake, D. R.,  
Brailsford, G., Brovkin, V., Bruhwiler, L., Crevoisier, C., Crill, P., Covey, K., Curry, C., Frankenberg, C., Gedney, N., Höglund-Isaksson,  
615 L., Ishizawa, M., Ito, A., Joos, F., Kim, H.-S., Kleinen, T., Krummel, P., Lamarque, J.-F., Langenfelds, R., Locatelli, R., Machida, T.,  
Maksyutov, S., McDonald, K. C., Marshall, J., Melton, J. R., Morino, I., Naik, V., O’Doherty, S., Parmentier, F.-J. W., Patra, P. K., Peng,  
C., Peng, S., Peters, G. P., Pison, I., Prigent, C., Prinn, R., Ramonet, M., Riley, W. J., Saito, M., Santini, M., Schroeder, R., Simpson, I. J.,  
Spahni, R., Steele, P., Takizawa, A., Thornton, B. F., Tian, H., Tohjima, Y., Viovy, N., Voulgarakis, A., Van Weele, M., Van Der Werf,  
G. R., Weiss, R., Wiedinmyer, C., Wilton, D. J., Wiltshire, A., Worthy, D., Wunch, D., Xu, X., Yoshida, Y., Zhang, B., Zhang, Z., and Zhu,  
620 Q.: The global methane budget 2000–2012, *Earth Syst. Sci. Data*, 8, 697–751, <https://doi.org/10.5194/essd-8-697-2016>, 2016.
- Saunois, M., Stavert, A. R., Poulter, B., Bousquet, P., Canadell, J. G., Jackson, R. B., Raymond, P. A., Dlugokencky, E. J., Houweling, S.,  
Patra, P. K., Ciais, P., Arora, V. K., Bastviken, D., Bergamaschi, P., Blake, D. R., Brailsford, G., Bruhwiler, L., Carlson, K. M., Carrol,  
M., Castaldi, S., Chandra, N., Crevoisier, C., Crill, P. M., Covey, K., Curry, C. L., Etiope, G., Frankenberg, C., Gedney, N., Heggin,  
M. I., Höglund-Isaksson, L., Hugelius, G., Ishizawa, M., Ito, A., Janssens-Maenhout, G., Jensen, K. M., Joos, F., Kleinen, T., Krummel,  
625 P. B., Langenfelds, R. L., Laruelle, G. G., Liu, L., Machida, T., Maksyutov, S., McDonald, K. C., McNorton, J., Miller, P. A., Melton,  
J. R., Morino, I., Müller, J., Murguía-Flores, F., Naik, V., Niwa, Y., Noce, S., O’Doherty, S., Parker, R. J., Peng, C., Peng, S., Peters, G. P.,  
Prigent, C., Prinn, R., Ramonet, M., Regnier, P., Riley, W. J., Rosentretter, J. A., Segers, A., Simpson, I. J., Shi, H., Smith, S. J., Steele, L. P.,  
Thornton, B. F., Tian, H., Tohjima, Y., Tubiello, F. N., Tsuruta, A., Viovy, N., Voulgarakis, A., Weber, T. S., van Weele, M., van der Werf,  
G. R., Weiss, R. F., Worthy, D., Wunch, D., Yin, Y., Yoshida, Y., Zhang, W., Zhang, Z., Zhao, Y., Zheng, B., Zhu, Q., Zhu, Q., and Zhuang,  
630 Q.: The Global Methane Budget 2000–2017, *Earth System Science Data*, 12, 1561–1623, <https://doi.org/10.5194/essd-12-1561-2020>,  
2020.
- Schaefer, H., Schaefer, H., Fletcher, S. E. M., Veidt, C., Lassey, K. R., Brailsford, G. W., Bromley, M., Dlugokencky, E. J., Michel, S. E.,  
Miller, J. B., Levin, I., Lowe, D. C., Martin, J., Vaughn, B. H., and White, J. W. C.: A 21st century shift from fossil-fuel to biogenic  
methane emissions indicated by  $^{13}\text{CH}_4$ , *Science*, 2705, 1–10, 2016.
- Schuldts, K. N., Aalto, T., Andrews, A., Aoki, S., Arduini, J., Baier, B., Bergamaschi, P., Biermann, T., Biraud, S. C., Boenisch, H., Brailsford,  
G., Chen, H., Colomb, A., Conil, S., Cristofanelli, P., Cuevas, E., Daube, B., Davis, K., Mazière, M. D., Delmotte, M., Desai, A., DiGangi,  
J. P., Dlugokencky, E., Elkins, J. W., Emmenegger, L., Fischer, M. L., Gatti, L. V., Gehrlein, T., Gerbig, C., Gloor, E., Goto, D., Haszpra,  
L., Hatakka, J., Heimann, M., Heliasz, M., Hermanssen, O., Hintsa, E., Holst, J., Ivakhov, V., Jaffe, D., Joubert, W., Kang, H.-Y., Karion,  
A., Kazan, V., Keronen, P., Ko, M.-Y., Kominkova, K., Kort, E., Kozlova, E., Krummel, P., Kubistin, D., Labuschagne, C., Langenfelds,  
640 R., Laurent, O., Laurila, T., Lauvaux, T., Lee, J., Lee, H., Lee, C.-H., Lehner, I., Leppert, R., Leuenberger, M., Lindauer, M., Loh, Z.,  
Lopez, M., Machida, T., Mammarella, I., Manca, G., Marek, M. V., Martin, M. Y., Matsueda, H., McKain, K., Miles, N., Miller, C. E.,  
Miller, J. B., Moore, F., Morimoto, S., Munro, D., Myhre, C. L., Mölder, M., Müller-Williams, J., Nichol, S., Niwa, Y., O’Doherty, S.,  
Obersteiner, F., Piacentino, S., Pichon, J. M., Pittman, J., Plass-Duelmer, C., Ramonet, M., Richardson, S., Rivas, P. P., Saito, K., Santoni,  
G., Sasakawa, M., Scheeren, B., Schuck, T., Schumacher, M., Seifert, T., Sha, M. K., Shepson, P., Sloop, C. D., Smith, P., Steinbacher,  
645 M., Stephens, B., Sweeney, C., Timas, H., Torn, M., Trisolino, P., Turnbull, J., Tørseth, K., Viner, B., Vitkova, G., Watson, A., Wofsy, S.,



- Worsey, J., Worthy, D., Zahn, A., and di Sarra, A. G.: Multi-laboratory compilation of atmospheric methane data for the period 1983-2020; obspack\_ch4\_1\_GLOBALVIEWplus\_v4.0\_2021-10-14, <https://doi.org/http://doi.org/10.25925/20211001>, 2021.
- 650 Sheng, J., Tunnicliffe, R., Ganesan, A. L., Maasackers, J. D., Shen, L., Prinn, R. G., Song, S., Zhang, Y., Scarpelli, T., Bloom, A. A., Rigby, M., Manning, A. J., Parker, R. J., Boesch, H., Lan, X., Zhang, B., Zhuang, M., and Lu, X.: Sustained methane emissions from China after 2012 despite declining coal production and rice-cultivated area, *Environmental Research Letters*, 16, 104018, <https://doi.org/10.1088/1748-9326/ac24d1>, 2021.
- 655 Sherwen, T., Schmidt, J. A., Evans, M. J., Carpenter, L. J., Großmann, K., Eastham, S. D., Jacob, D. J., Dix, B., Koenig, T. K., Sinreich, R., Ortega, I., Volkamer, R., Saiz-Lopez, A., Prados-Roman, C., Mahajan, A. S., and Ordóñez, C.: Global impacts of tropospheric halogens (Cl, Br, I) on oxidants and composition in GEOS-Chem, *Atmospheric Chemistry and Physics*, 16, 12 239–12 271, <https://doi.org/10.5194/acp-16-12239-2016>, 2016.
- Sherwood, O. A., Schwietzke, S., Arling, V. A., and Etiope, G.: Global inventory of gas geochemistry data from fossil fuel, microbial and burning sources, version 2017, *Earth System Science Data*, 9, 639–656, <https://doi.org/10.5194/essd-9-639-2017>, 2017.
- Snover, A. K. and Quay, P. D.: Hydrogen and carbon kinetic isotope effects during soil uptake of atmospheric methane, *Global Biogeochemical Cycles*, 14, 25–39, <https://doi.org/10.1029/1999GB900089>, 2000.
- 660 Source: European Commission, J. R. C. J. E. A. A. P.: Emission Database for Global Atmospheric Research (EDGAR), release version 4.2., <http://edgar.jrc.ec.europa.eu>, 2011.
- Steele, L. P., Fraser, P. J., Rasmussen, R. A., Khalil, M. A. K., Conway, T. J., Crawford, A. J., Gammon, R. H., Masarie, K. A., and Thoning, K. W.: *The Global Distribution of Methane in the Troposphere*, pp. 417–463, Springer Netherlands, 1987.
- Turner, A. J., Frankenberg, C., Wennberg, P. O., and Jacob, D. J.: Ambiguity in the causes for decadal trends in atmospheric methane and hydroxyl, *Proceedings of the National Academy of Sciences*, 114, 5367–5372, <https://doi.org/10.1073/pnas.1616020114>, 2017.
- 665 Turner, A. J., Frankenberg, C., and Kort, E. A.: Interpreting contemporary trends in atmospheric methane, *Proceedings of the National Academy of Sciences*, 116, 201814 297, <https://doi.org/10.1073/pnas.1814297116>, 2019.
- Vaughn, B., Miller, J., Ferretti, D., and White, J.: Stable isotope measurements of atmospheric CO<sub>2</sub> and CH<sub>4</sub>, *Handbook of Stable Isotope Analytical Techniques*, vol 1, chap. 14, Elsevier, 2004.
- 670 Voulgarakis, A., Naik, V., Lamarque, J.-F., Shindell, D. T., Young, P. J., Prather, M. J., Wild, O., Field, R. D., Bergmann, D., Cameron-Smith, P., Cionni, I., Collins, W. J., Dalsøren, S. B., Doherty, R. M., Eyring, V., Faluvegi, G., Folberth, G. A., Horowitz, L. W., Josse, B., McKenzie, I. A., Nagashima, T., Plummer, D. A., Righi, M., Rumbold, S. T., Stevenson, D. S., Strode, S. A., Sudo, K., Szopa, S., and Zeng, G.: Analysis of present day and future OH and methane lifetime in the ACCMIP simulations, *Atmos. Chem. Phys.*, 13, 2563–2587, <https://doi.org/10.5194/acp-13-2563-2013>, 2013.
- 675 Wilson, C., Chipperfield, M. P., Gloor, M., Parker, R. J., Boesch, H., McNorton, J., Gatti, L. V., Miller, J. B., Basso, L. S., and Monks, S. A.: Large and increasing methane emissions from eastern Amazonia derived from satellite data, 2010–2018, *Atmospheric Chemistry and Physics*, 21, 10 643–10 669, <https://doi.org/10.5194/acp-21-10643-2021>, 2021.
- Worden, J., Bloom, A., Pandey, S., Jiang, Z., Worden, H., Walker, T., Houweling, S., and Röckmann, T.: Reduced biomass burning emissions reconcile conflicting estimates of the post-2006 atmospheric methane budget, *Nature Communications*, 8, <https://doi.org/10.1038/s41467-017-02246-0>, 2017.
- 680 Yin, Y., Chevallier, F., Ciais, P., Bousquet, P., Saunois, M., Zheng, B., Worden, J., Bloom, A. A., Parker, R. J., Jacob, D. J., Dlugokencky, E. J., and Frankenberg, C.: Accelerating methane growth rate from 2010 to 2017: leading contributions from the tropics and East Asia, *Atmospheric Chemistry and Physics*, 21, 12 631–12 647, <https://doi.org/10.5194/acp-21-12631-2021>, 2021.

- Zazzeri, G., Lowry, D., Fisher, R. E., France, J. L., Lanoisellé, M., Kelly, B. F. J., Necki, J. M., Iverach, C. P., Ginty, E., Zimnoch, M., Jasek, A., and Nisbet, E. G.: Carbon isotopic signature of coal-derived methane emissions to the atmosphere: from coalification to alteration, *Atmospheric Chemistry and Physics*, 16, 13 669–13 680, <https://doi.org/10.5194/acp-16-13669-2016>, 2016.
- Zhao, Y., Saunio, M., Bousquet, P., Lin, X., Berchet, A., Hegglin, M. I., Canadell, J. G., Jackson, R. B., Hauglustaine, D. A., Szopa, S., Stavert, A. R., Abraham, N. L., Archibald, A. T., Bekki, S., Deushi, M., Jöckel, P., Josse, B., Kinnison, D., Kirner, O., Marécal, V., O'Connor, F. M., Plummer, D. A., Revell, L. E., Rozanov, E., Stenke, A., Strode, S., Tilmes, S., Dlugokencky, E. J., and Zheng, B.: Inter-model comparison of global hydroxyl radical (OH) distributions and their impact on atmospheric methane over the 2000–2016 period, *Atmospheric Chemistry and Physics*, 19, 13 701–13 723, <https://doi.org/10.5194/acp-19-13701-2019>, 2019.
- Zhou, L., Kitzis, D., and Tans, P.: Report of the Fourth WMO Round-Robin Reference Gas Intercomparison, 2002-2007, Tech. rep., World Meteorological Organisation, 2009.

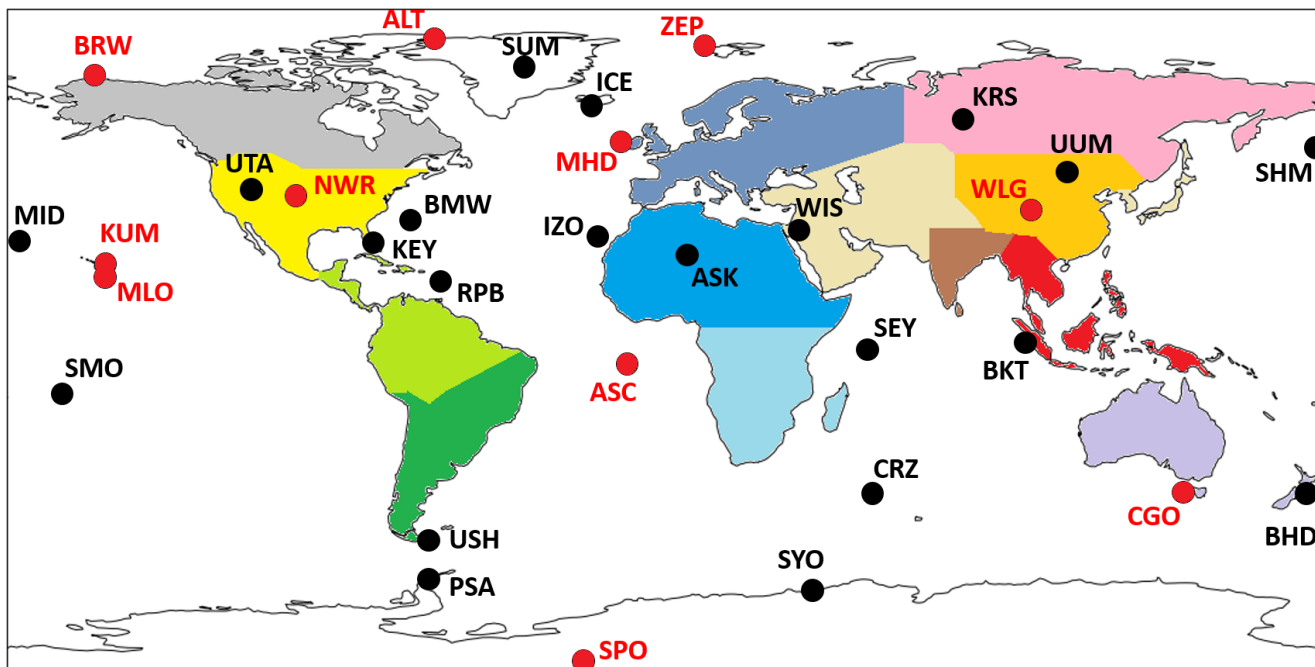


**Figure 1.** Map showing regions that are optimised in the CH<sub>4</sub> and δ<sup>13</sup>C inversions, in different colours. Black dots and labels show the location of ground-based in-situ measuring measurement sites that measure CH<sub>4</sub> mole fraction. Red dots and labels indicate both total-mole fraction CH<sub>4</sub> and δ<sup>13</sup>C measuring sites. Regions are named as follows: Grey - North American Boreal; Yellow - North American Temperate; Light Green - South American Tropical; Dark Green - South American Temperate; Purple - Europe; Blue - North Africa; Light Blue - Southern Africa; Pink - Boreal Eurasia; Orange - China; Brown - India; Peach - Temperate Eurasia; Red - Tropical SE Asia; Lilac - Oceania; White - Oceans. Site identifiers are detailed in Table A2.

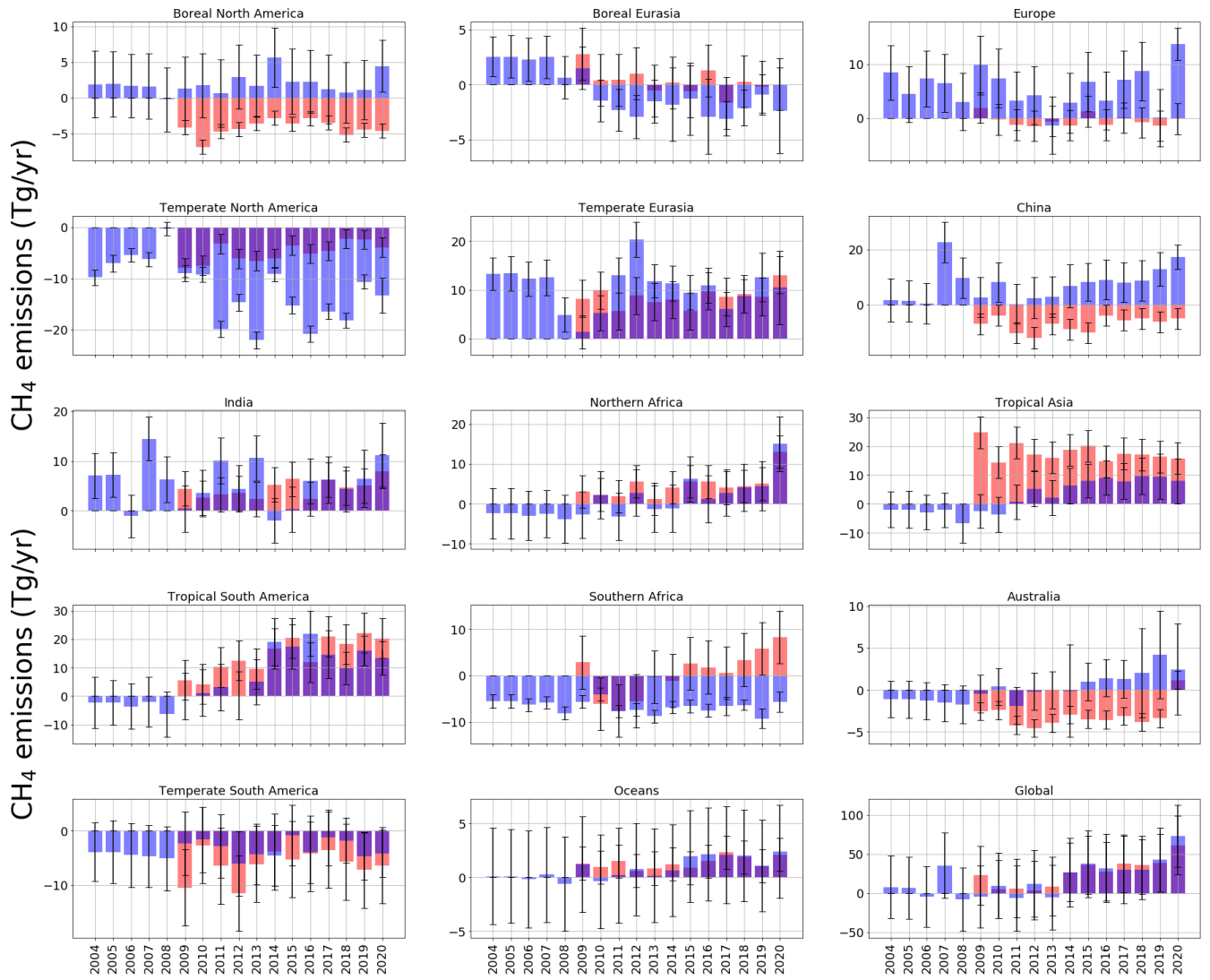


**Figure 2.** Annual mean CH<sub>4</sub> *a posteriori* emissions estimates as a residual value relative to a priori (Tg/yr) from each of the inversion regions in latitudinal order (geographic coverage indicated by Figure 1), for both ground-based and GOSAT inversion results. ~~The emissions are shown as a residual value, relative to the a priori yearly emission for each region.~~ Uncertainties ~~in yearly emissions~~ are indicated, as calculated from inversion calculations, with a *a priori* uncertainty of 50% for the in-situ ground-based results and 60% for the GOSAT results. The ground-based *a posteriori* is in blue; the GOSAT *a posteriori* are in red.

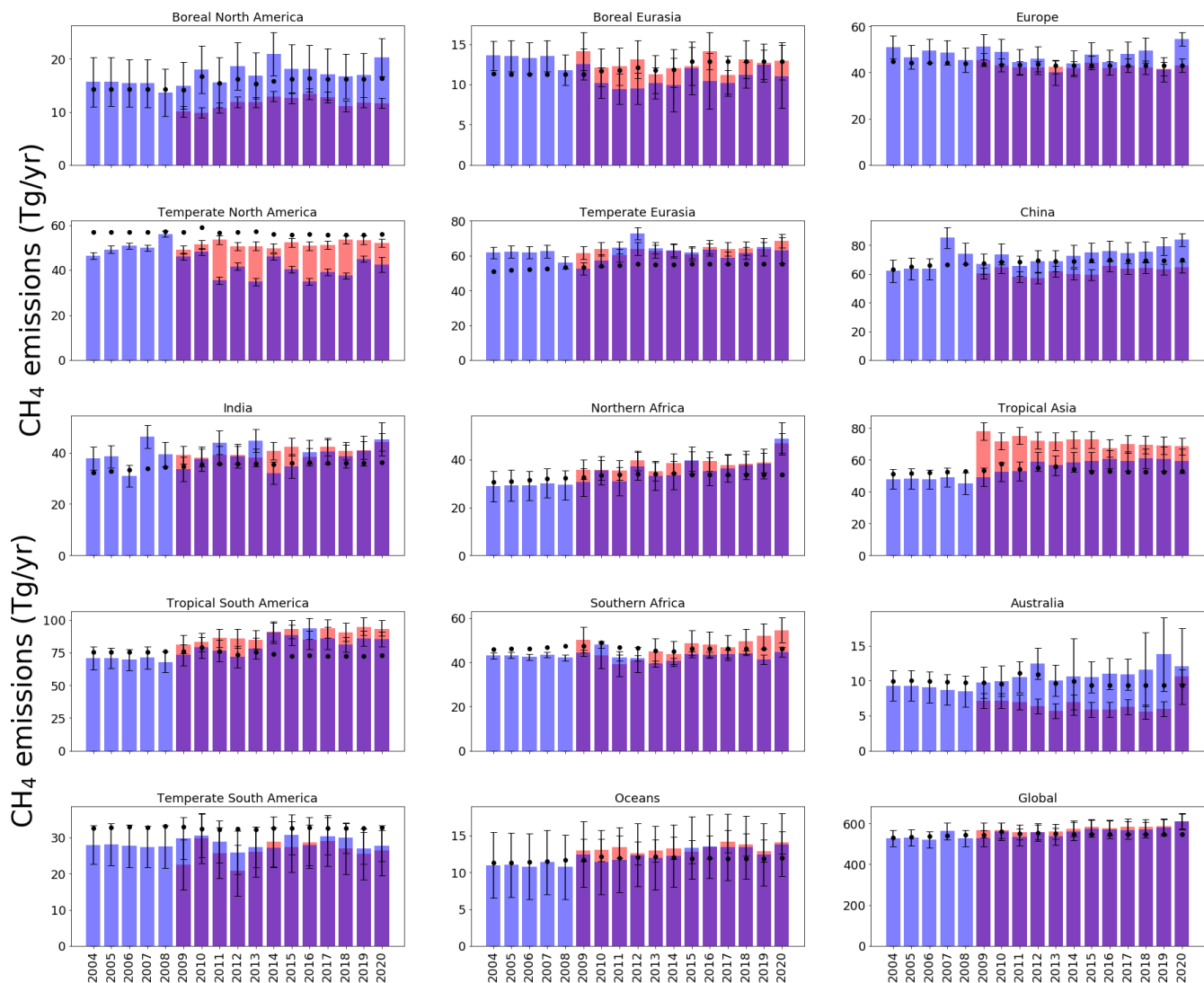


**Figure 3.** *A posteriori* emissions estimates (Tg/yr) inferred from ground-based *in situ* data (blue) and GOSAT data (red, with record starting in 2010) for the geographical regions shown by Figure 1. *A priori* emissions estimates are denoted by black dots and *a posteriori* uncertainties are denoted by whisker bars.

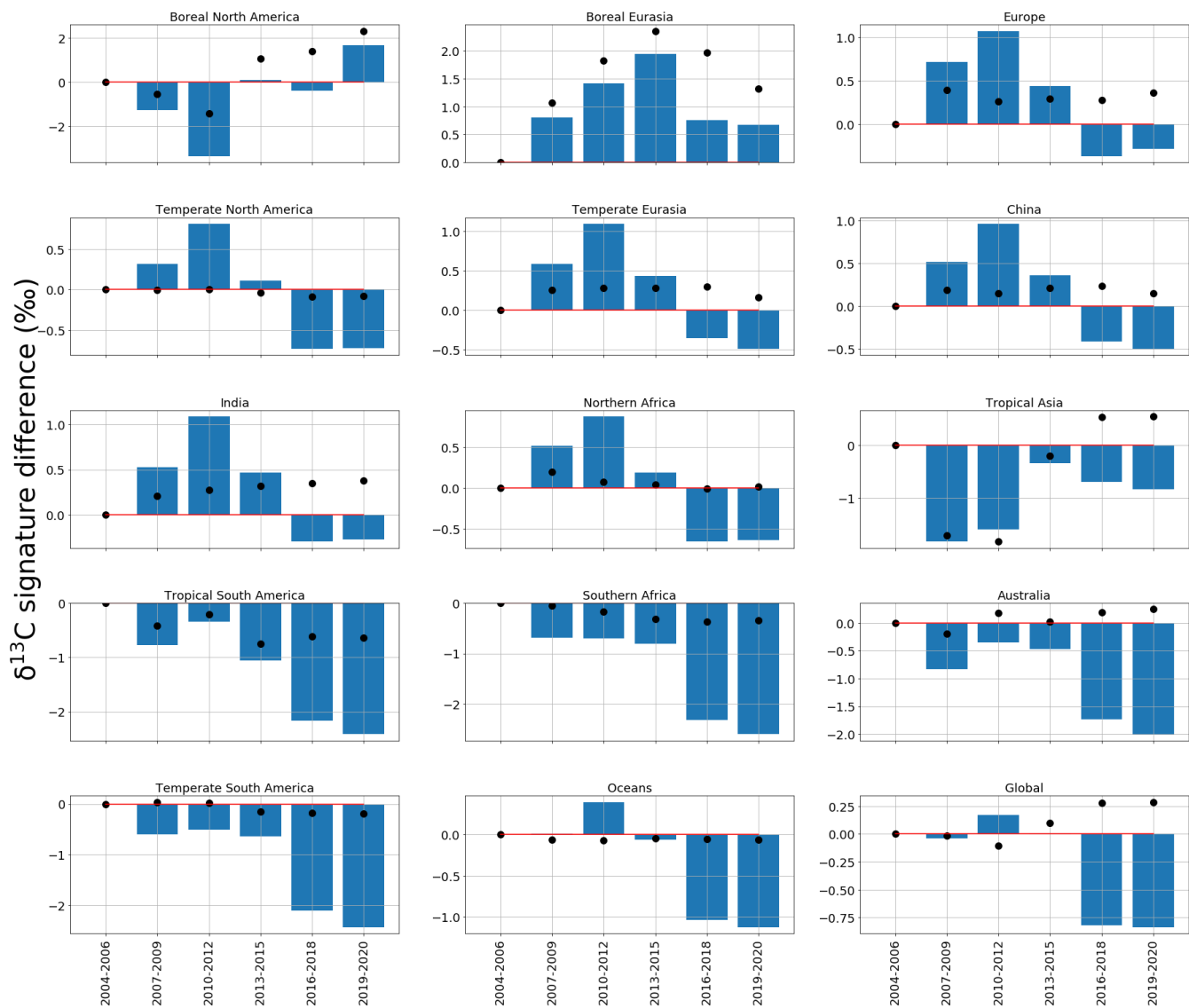
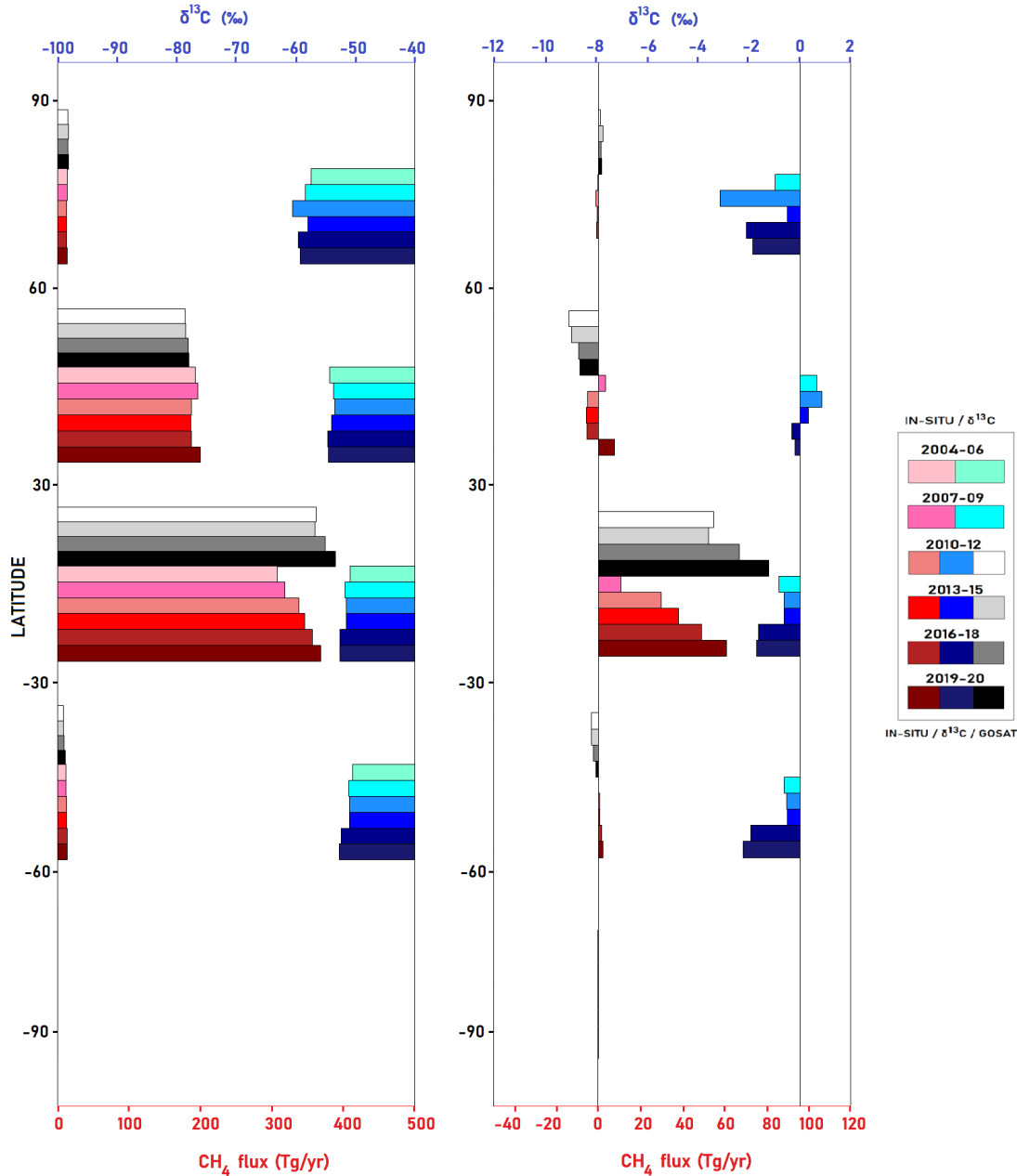


**Figure 4.** Regional and global *a posteriori*  $\delta^{13}\text{C}$  emissions source signatures (‰), in three-yearly groups (2004-06, 2007-09, 2010-12, 2013-15, 2016-18, 2019-20) as a residual from the 2004-06 *a posteriori* regional emissions source signature value. The *a priori* equivalent is represented by black dots. The regions are those solved for in the  $\text{CH}_4$  and  $\delta^{13}\text{C}$  inversions and are indicated by Figure 1.





A-posteriori emissions estimates. The colours of each x axis are indicative of the results to which they refer (Tg/yr) inferred from ground-based in situ data (i.e. blue) and GOSAT data (upper axis for δ<sup>13</sup>C results, red, with record starting in 2010) lower axis for the geographical regions shown by Figure 1. A priori CH<sub>4</sub> emissions estimates are denoted by black dots and a posteriori uncertainties are denoted by whisker bars results).

A-posteriori emissions estimates. The colours of each x axis are indicative of the results to which they refer (Tg/yr) inferred from ground-based in situ data (i.e. blue) and GOSAT data (upper axis for δ<sup>13</sup>C results, red, with record starting in 2010) lower axis for the geographical regions shown by Figure 1. A priori CH<sub>4</sub> emissions estimates are denoted by black dots and a posteriori uncertainties are denoted by whisker bars results).

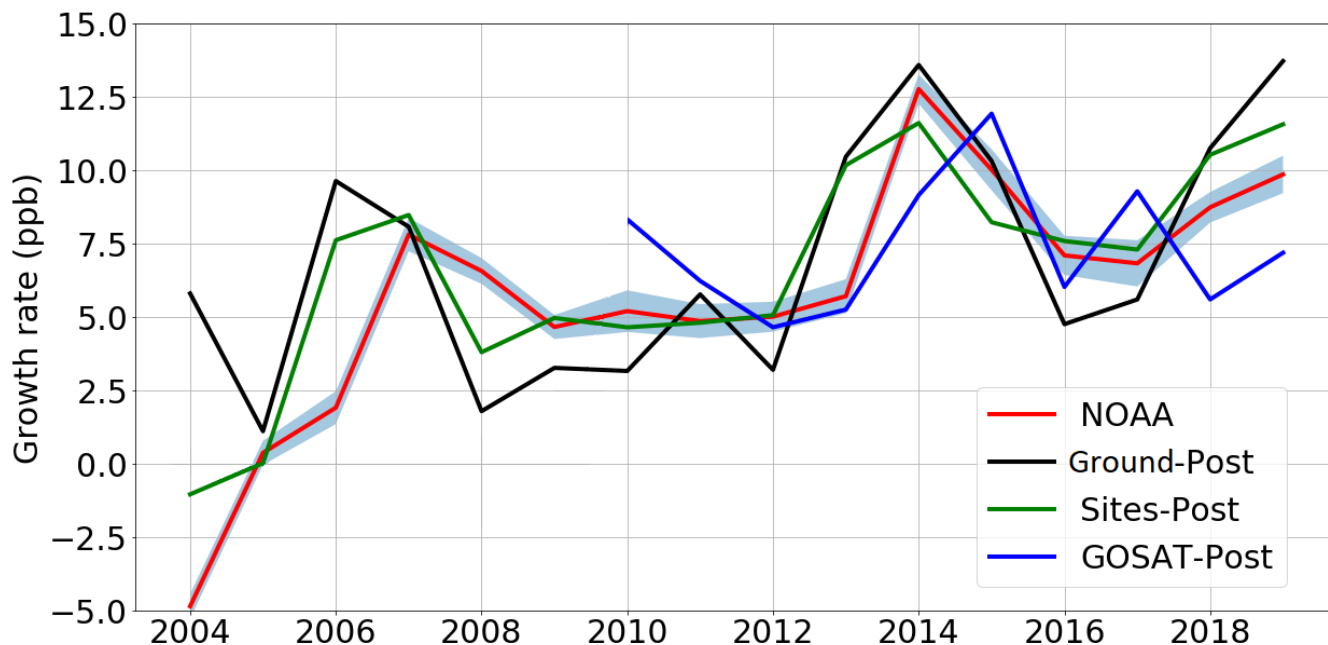


**Figure 6.** *A posteriori* annual mean atmospheric CH<sub>4</sub> growth rate inferred from *in situ* (black line) and GOSAT data (blue line) compared with the equivalent data as published by NOAA (red line, [with uncertainty as blue surrounding field](#), Dlugokencky et al., 2020). The green line denotes the annual atmospheric growth rate determined using the *in situ* mole fraction data from the sites included in the inversion ( $\pm$  Sites-Post'). To calculate the atmospheric growth rates from model calculations (NOAA-Post-Ground-Post and GOSAT-Post), we compare the average global CH<sub>4</sub> mole fraction in one year (the mean mole fraction of every grid [square-box](#) in every month of a year), with the mean value from the following year. The calculation is January-January, in order to remove the effects of the seasonal cycle, following the approach by NOAA (Dlugokencky et al., 2020).

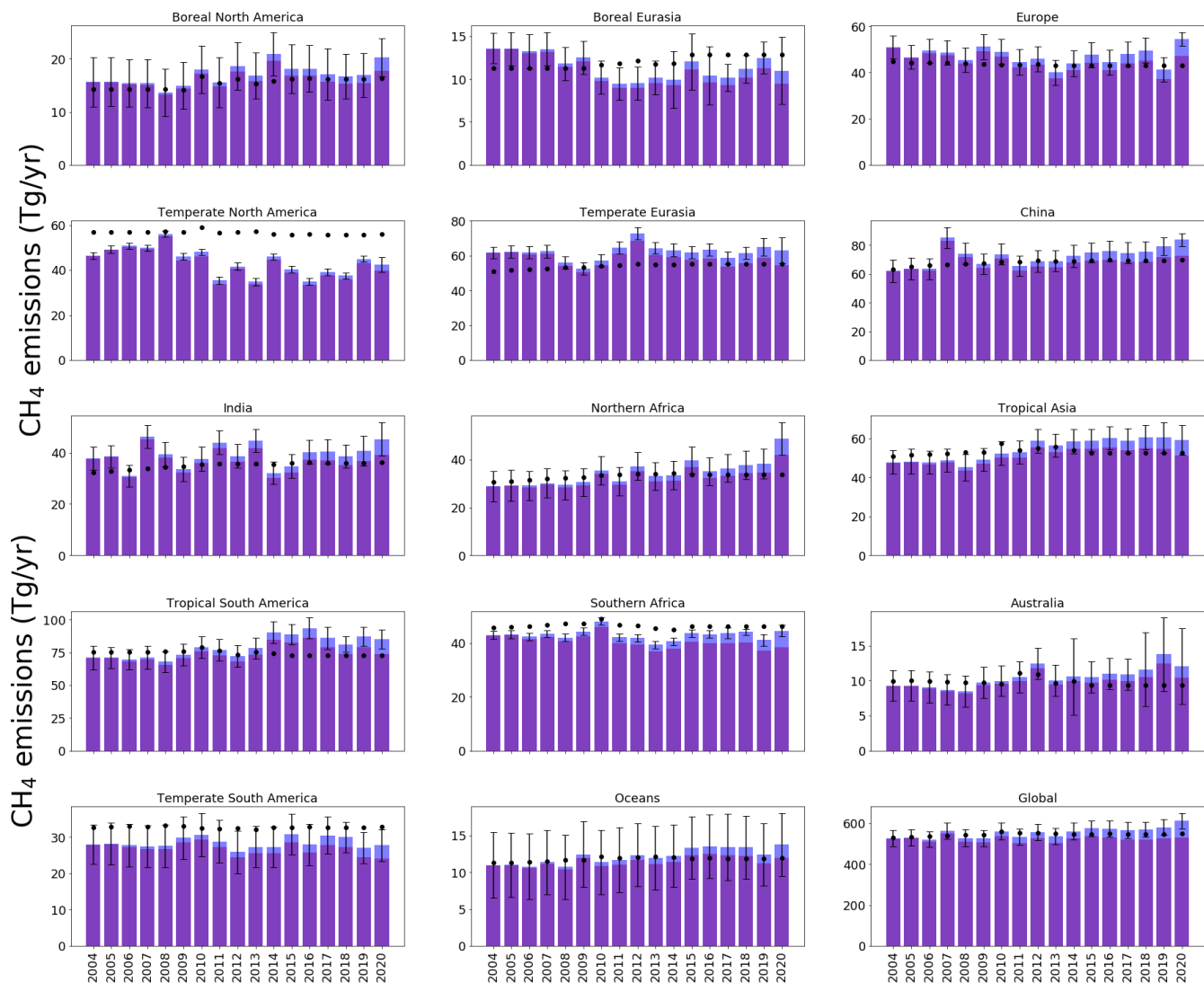


**Figure 7.** Annual mean CH<sub>4</sub> emissions (Tg/yr) for each region of the inversion (indicated by Figure 1) inferred from the ground-based data (dark blue) and the emissions estimates determined by a reduced OH values (described in the text, shown in red). *A priori* regional emissions estimates are indicated by black dots. Regional uncertainties for the *a posteriori* emissions are indicated.

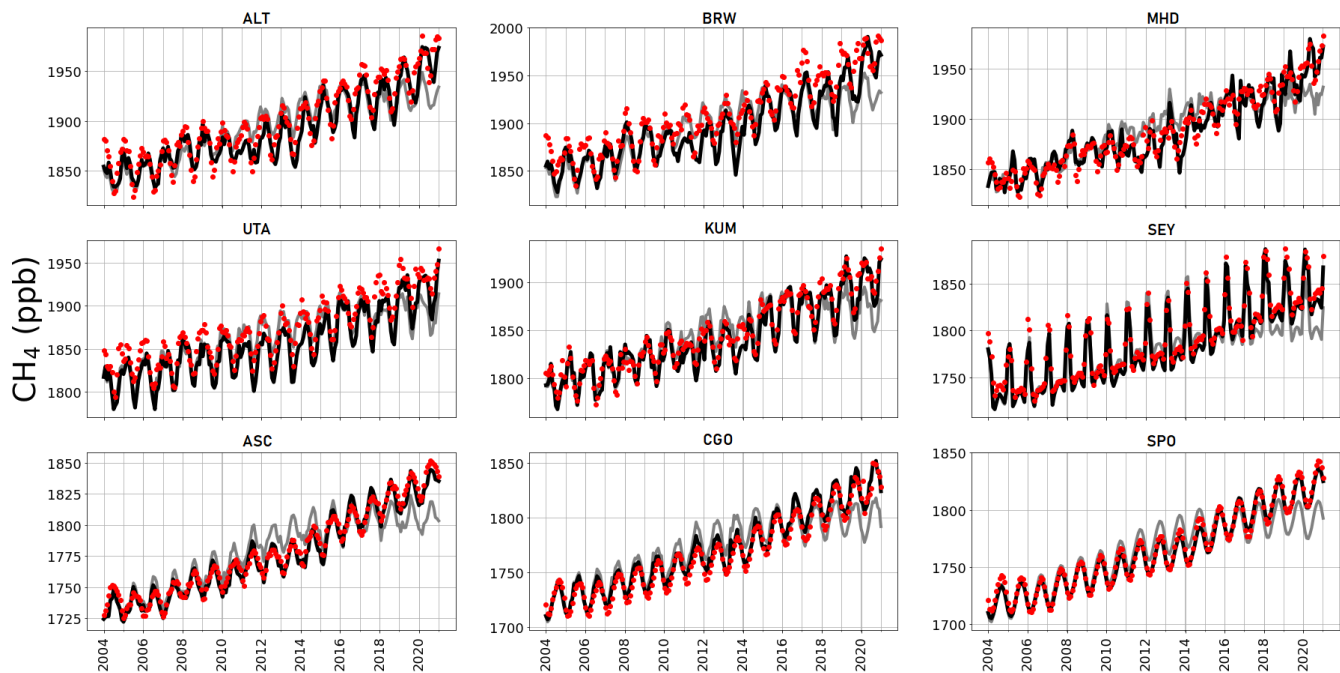


**Figure A1.** Observed (red dots), and *a priori* (grey), *a posteriori* (black) model atmospheric mole fractions at a series of NOAA sites (subplot titles denote site codes, Table A2), covering a range of latitudes.

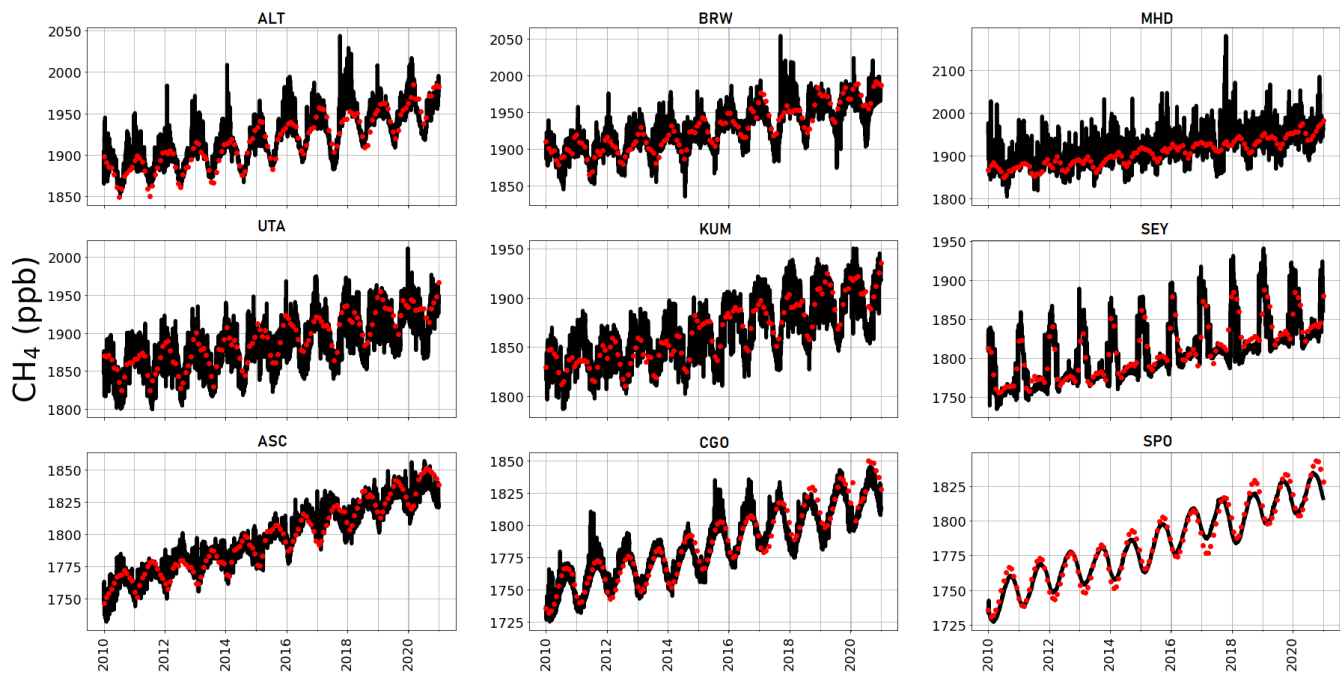


**Figure A2.** Observed (red dots), and three-hourly surface *a posteriori* CH<sub>4</sub> values inferred from GOSAT data (black) at the location of a number of NOAA sites (Table A2) 2010-2020.

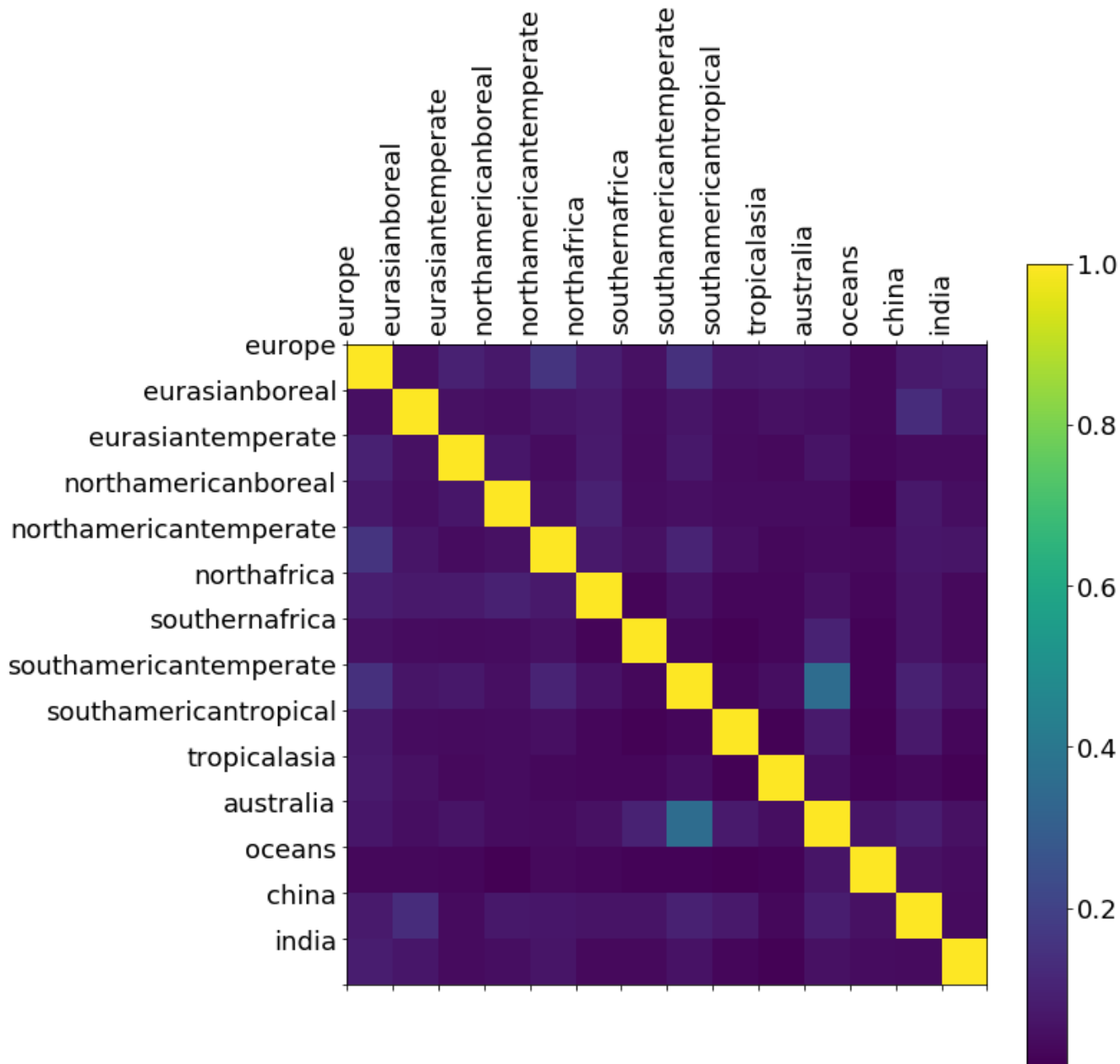


**Figure A3.** *A posteriori* correlations between CH<sub>4</sub> emissions from geographical regions inferred from NOAA [ground-based](#) CH<sub>4</sub> mole fraction data. These correlations are determined by normalising the diagonal elements of the *a posteriori* error covariance matrix (Eq. (2)).

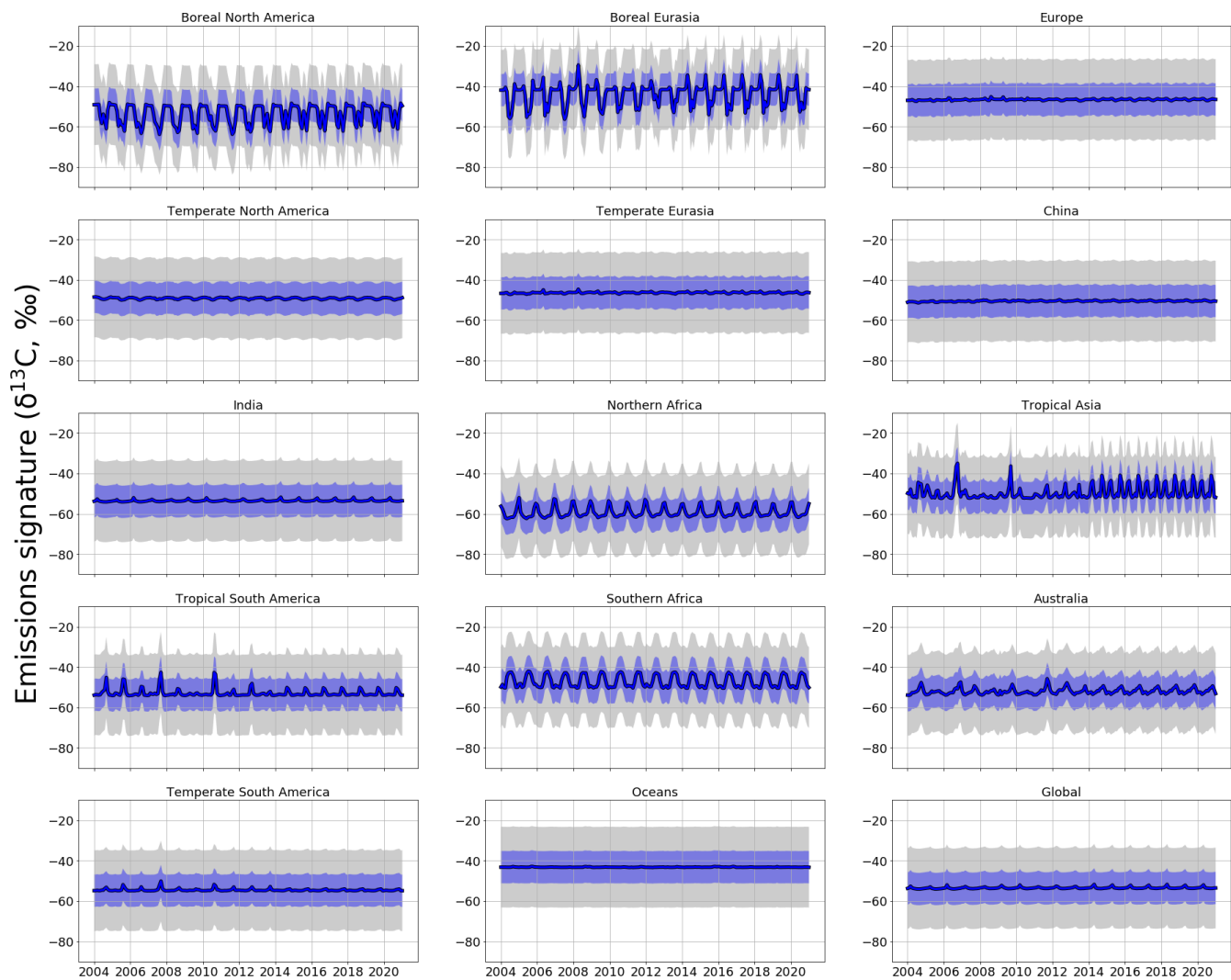


**Figure A4.** Monthly *a priori* (grey) and *a posteriori* (blue) regional  $\delta^{13}\text{C}$  source signatures (‰). Values are produced using ground-based *in situ*  $\delta^{13}\text{C}$  data. Uncertainties in source signatures are indicated as shaded envelopes, with *a priori* uncertainties of 15 ‰.

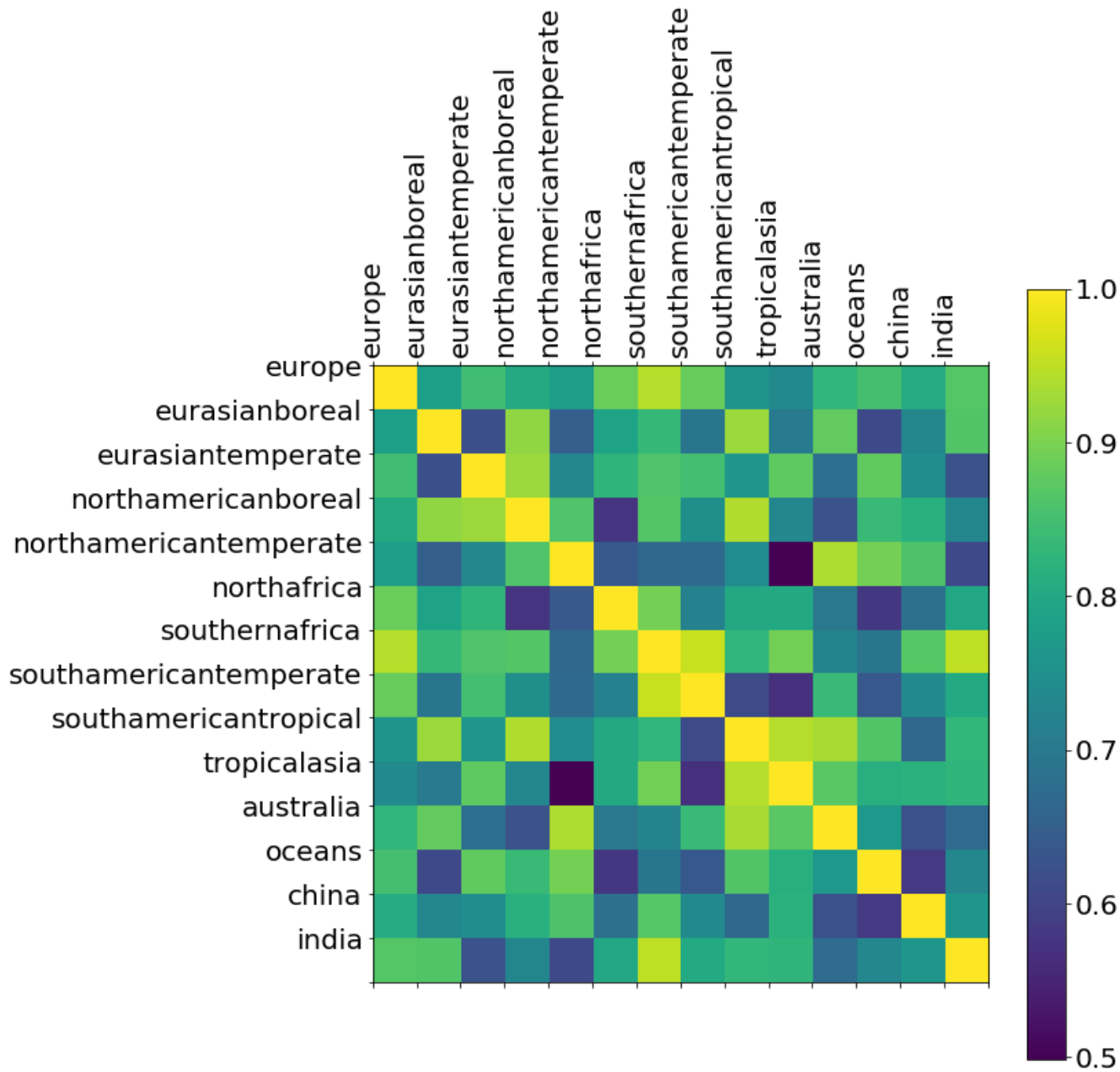


**Figure A5.** *A posteriori* correlations between  $\delta^{13}\text{C}$  source signatures from geographical regions inferred from ground-based  $\delta^{13}\text{C}$  data. These correlations are determined by normalising the diagonal elements of the *a posteriori* error covariance matrix (Equation 2).



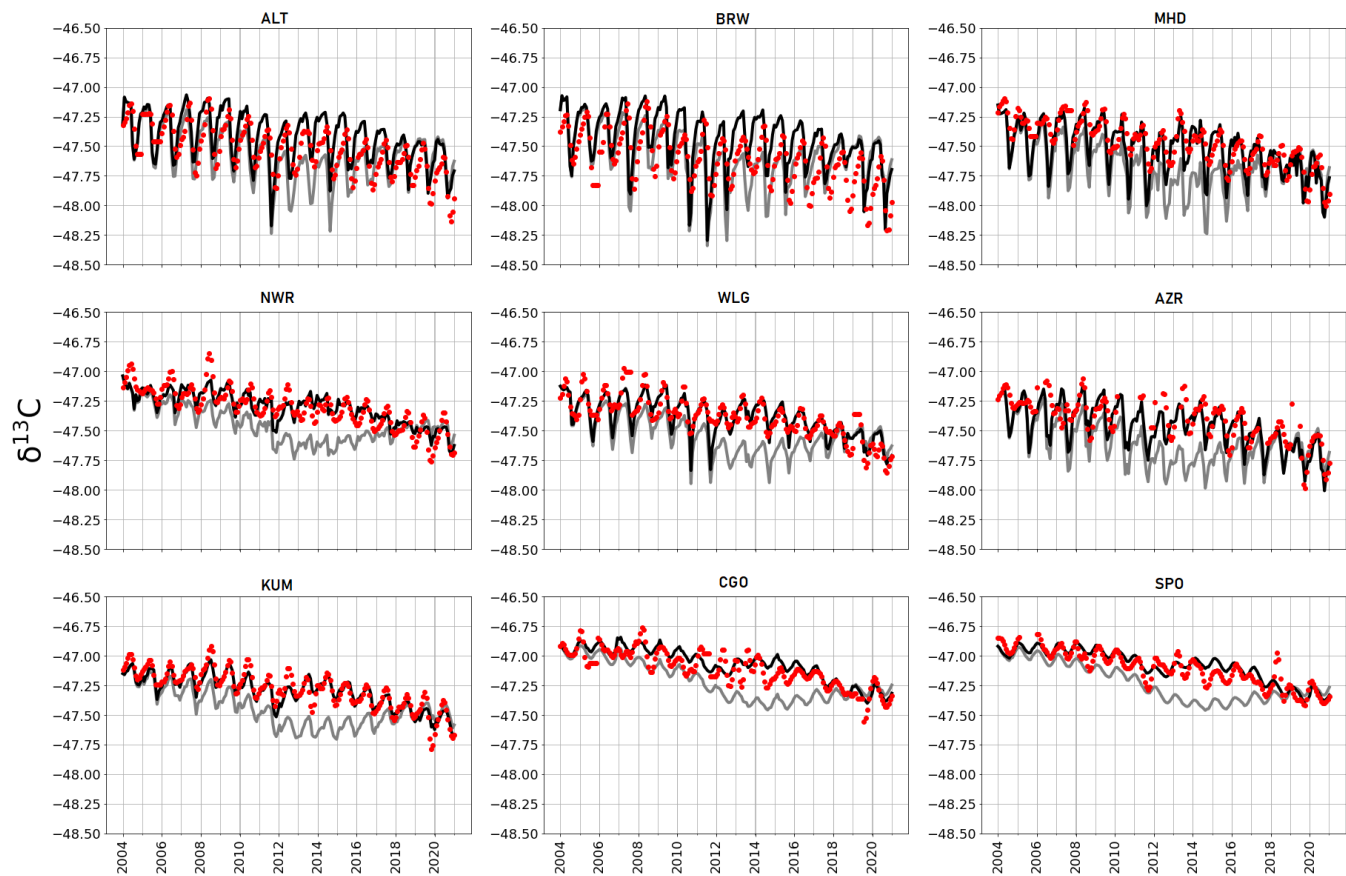


**Figure A6.** *A priori* (grey) and *a posteriori* (black) monthly estimates of atmospheric  $\delta^{13}\text{C}$ , simulated at NOAA sites across latitudes (site codes listed in Table A2). Red dots indicate monthly mean  $\delta^{13}\text{C}$  data from CU-INSTAAR for the respective sites.

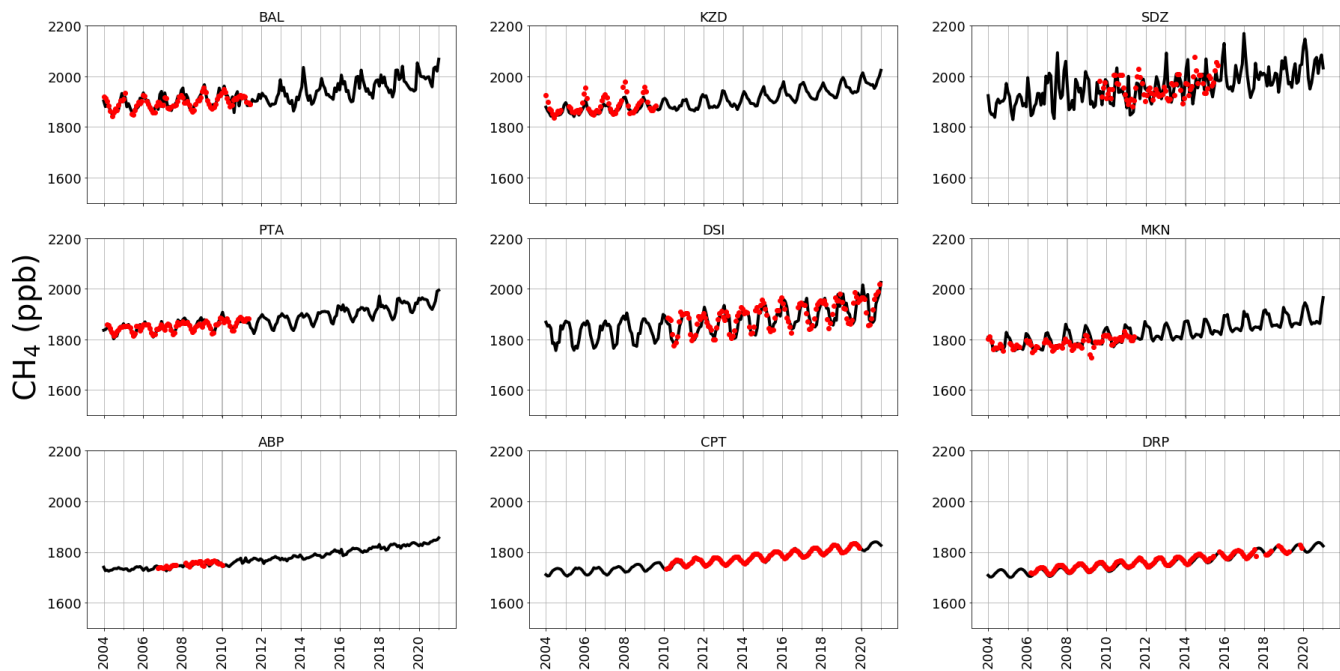


**Figure A7.** *A posteriori* (black) monthly estimates of atmospheric CH<sub>4</sub>, simulated at NOAA sites across latitudes. Red dots indicate monthly mean CH<sub>4</sub> data from the NOAA network sites indicated. These sites were not included in the CH<sub>4</sub> inversion, but are shown here to provide independent validation of *a posteriori* emissions. The sites included are: Baltic Sea, Poland (55.35°N, 17.22°E); Sary Taukum, Kazakhstan (44.08°N, 76.87°E); Shangdianzi, China (44.65°N, 117.12°E); Point Arena, USA (38.95°N, 123.74°W); Dongsha Island, Taiwan (20.70°N, 116.73°E); Mt Kenya, Kenya (0.06°S, 37.29°E); Arembepe, Brazil (12.77°S, 38.17°W); Cape Point, South Africa (34.35°S, 18.49°E); Drake Passage (59.00°S, 64.69°W).

**Table 1.** ~~Magnitudes~~ Global mean emissions of different CH<sub>4</sub> source types from bottom-up inventories (Saunois et al., 2020) and the corresponding conventional isotope ratios signatures (Sherwood et al., 2017). ~~Magnitudes~~ Uncertainties are ~~from bottom-up inventories~~ (Saunois et al., 2016), ~~with uncertainties shown~~ as max-min values in square brackets.

Source Type	Annual Mean Emission 2003-2012 (Tg/CH <sub>4</sub> )	Isotopic Ratio $\delta^{13}\text{C}_p$ (‰)
Gas and Oil	<del>79-80</del> [69-88] <del>68-92</del>	-44.0 [ $\pm$ 10.7]
Coal	<del>41-42</del> [26-50] <del>29-61</del>	-49.5 [ $\pm$ 11.2]
Livestock	<del>106-111</del> [97-11] <del>106-116</del>	-65.4 [ $\pm$ 6.7]
Waste	<del>195-65</del> [178-206] <del>60-69</del>	-56.0 [ $\pm$ 7.6]
Biomass Burning	<del>18-17</del> [15-20] <del>14-26</del>	-26.2 [ $\pm$ 4.8]
Termites	9 [3-15]	-63.4 [ $\pm$ 6.4]
Wetlands	<del>185-149</del> [153-227] <del>102-182</del>	-61.5 [ $\pm$ 5.4] (Tropical) -71.5 [ $\pm$ 5.4] (Arctic)
Rice	30 [ <del>27-35</del> <del>25-38</del> ]	-62.2 [ $\pm$ 3.9]

**Table A1.** Kinetic Isotope Effects (KIEs) for different isotopologues reacting with the three main sinks of CH<sub>4</sub> (OH, Cl, soil) at [298K](#) [298 K](#). A KIE indicates relative reaction rate compared with <sup>12</sup>CH<sub>4</sub>; the reaction rate constant is applied to the OH and Cl sinks and is dependent upon temperature (T); and the scaling factor is applied to the soil sink at each timestep (handled as a negative emission).

Isotopologue	Sink	KIE	Reaction Rate Constant	Scaling Factor	Literature Source
<sup>12</sup> CH <sub>4</sub>	OH	1	$2.45 \times 10^{-12} \times e^{\frac{-1775}{T}}$	n/a	Burkholder et al., 2019
<sup>12</sup> CH <sub>4</sub>	Cl	1	$9.600 \times 10^{-12} \times e^{\frac{-1360}{T}}$	n/a	Kirschke et al., 2013
<sup>12</sup> CH <sub>4</sub>	soil	n/a	n/a	1	Snover and Quay, 2000
<sup>13</sup> CH <sub>4</sub>	OH	1.0039	$2.44 \times 10^{-12} \times e^{\frac{-1775}{T}}$	n/a	Burkholder et al., 2019
<sup>13</sup> CH <sub>4</sub>	Cl	1.06	$9.057 \times 10^{-12} \times e^{\frac{-1360}{T}}$	n/a	Feilberg et al., 2005
<sup>13</sup> CH <sub>4</sub>	soil	n/a	n/a	1.0670	Snover and Quay, 2000

**Table A2.** Sites that are included in the *in situ* inversions. All sites are part of the NOAA network, other than KRS, which is part of the JR-STATION network, monitored by NIES Japan.

<b>Code</b>	<b>Full Name</b>	<b>Latitude</b>	<b>Longitude</b>
ALT	Alert Station	82.28	-62.30
ZEP	Ny-Alesund, Svalbard	78.90	11.89
SUM	Summit, Greenland	72.60	-38.42
BRW	Barrow Station	71.32	156.61
ICE	Storhofdi,Iceland	63.40	-20.29
KRS	Karasevoe, Siberia	58.14	82.25
MHD	Mace Head, Ireland	53.33	-9.90
SHM	Shemya Island, Alaska	52.71	174.12
UUM	Ulaan Uul, Mongolia	44.45	111.09
NWR	Niwot Ridge, Colorado	40.05	-105.59
UTA	Wendover, Utah	39.90	-113.72
WLG	Mt. Waliguan, China	36.29	100.90
BMW	Bermuda	32.26	-64.88
WIS	Ketura, Israel	29.96	35.06
IZO	Izana, Tenerife	28.31	-16.50
MID	Midway Islands	28.22	-177.37
KEY	Key Biscane, Florida	25.67	-80.16
ASK	Assekrem, Algeria	23.26	5.63
KUM	Cape Kumukahi, Hawaii	19.56	-154.89
MLO	Mauna Loa, Hawaii	19.54	-155.58
RPB	Ragged Point, Barbados	13.17	-59.43
SEY	Mahe Island, Seychelles	-4.68	55.53
ASC	Ascension Island	-7.97	-14.40
SMO	American Samoa	-14.25	-170.56
CGO	Cape Grim	-40.68	144.69
BHD	Baring Head	-41.40	174.87
CRZ	Crozet Island	-46.43	51.85
USH	Ushuaia, Argentina	-54.84	-68.31
PSA	Palmer Station, Antarctica	-64.77	-64.05
SYO	Syowa Station, Antarctica	-69.01	39.59
SPO	South Pole, Antarctica	-89.98	-24.8